electronics

MDPI

Article

On Unsupervised Artificial Intelligence-Assisted Design of Antennas for High-Performance Planar Devices

Slawomir Koziel [1,2,*], Weiping Dou [3], Peter Renner [3], Andrew Cohen [3], Yuandong Tian [3], Jiang Zhu [3] and Anna Pietrenko-Dabrowska [2]

[1] Engineering Optimization & Modeling Center, Reykjavik University, 102 Reykjavik, Iceland
[2] Faculty of Electronics, Telecommunications and Informatics, Gdansk University of Technology, 80-233 Gdansk, Poland; anna.dabrowska@pg.edu.pl
[3] Meta Platforms Technologies, LLC, Menlo Park, CA 94025, USA; wdou@meta.com (W.D.); peterrenner@meta.com (P.R.); andrewcohen@meta.com (A.C.); yuandong@meta.com (Y.T.); jiangzhu@meta.com (J.Z.)
* Correspondence: koziel@ru.is

Abstract: Designing modern antenna structures is a challenging endeavor. It is laborious and heavily reliant on engineering insight and experience, especially at the initial stages oriented towards the development of a suitable antenna architecture. Due to its interactive nature and hands-on procedures (mainly parametric studies) for validating the suitability of particular geometric setups, typical antenna development requires many weeks and significant involvement of a human expert. The same reasons only allow the designer to try out a very limited number of options in terms of antenna geometry arrangements. Automated topology development and dimension sizing is therefore of high interest, especially from an industry perspective where time-to-market and expert-related expenses are of paramount importance. This paper discusses a novel approach to unsupervised specification-driven design of planar antennas. The presented methodology capitalizes on a flexible and scalable antenna parameterization, which enables the realization of complex geometries while maintaining reasonably small parameter space dimensionality. A customized nature-inspired algorithm is employed to carry out space exploration and identification of a quasi-optimum antenna topology in a global sense. A fast gradient-based procedure is then incorporated to fine-tune antenna dimensions. The design framework works entirely in a black-box fashion with the only input being design specifications, and optional constraints, e.g., concerning the structure size. Numerous illustration case studies demonstrate the capability of the presented technique to generate unconventional antenna topologies of satisfactory performance using reasonable computational budgets, and with no human expert interaction necessary whatsoever.

Keywords: antenna design; unsupervised design; artificial intelligence; design automation; nature-inspired optimization; parameter tuning

Citation: Koziel, S.; Dou, W.; Renner, P.; Cohen, A.; Tian, Y.; Zhu, J.; Pietrenko-Dabrowska, A. On Unsupervised Artificial Intelligence-Assisted Design of Antennas for High-Performance Planar Devices. *Electronics* **2023**, *12*, 3462. https://doi.org/10.3390/electronics12163462

Academic Editor: Ikmo Park

Received: 27 July 2023
Revised: 7 August 2023
Accepted: 14 August 2023
Published: 15 August 2023

1. Introduction

We are imaging a world of new social experiences. In the metaverse, we can connect with people, play, and work in an online immersive experience. Virtual reality (VR) technology submerges us in 3D spaces that surpass the real world, allowing us to feel as if we were together with our families and friends. Augmented reality (AR) permits adding amusing virtual effects to photographs and videos, letting us express ourselves with the people who matter the most. On 6 May 2015, Facebook (now Meta) announced the first consumer version of Oculus Rift, and this AR headset was tethered with cables. The reason was obvious. Cutting-edge computer graphics require a bandwidth and responsiveness that only a wired connection could deliver at the moment. Wi-Fi 6E extends on the existent Wi-Fi 6 (802.11ax) standard and permits accessing the new 6 GHz band. This translates into 1200 MHz of pure spectrum in the United States, but also in the majority of the

outside world (with almost 500 MHz available in the European Union). It can provide data throughput up to 9.6 Gbps and an ultra-low latency of less than 3 ms. Consequently, it soon becomes an inevitable technology candidate to support high fidelity interaction for virtual and augmented reality.

The critical components of the aforementioned, and—for that matter—any wireless communication system, are antennas. In industry, the conventional design approach usually starts with an existing antenna geometric structure that can be found in previous generations of products and in publications, or inspired by engineers' prior knowledge. Next, the structure is adapted to the available antenna volume in the target devices, and possibly occupies the entire assigned space in order to maximize the antenna efficiency. Finally, the antenna design problem is formulated and solved to allow automated adjustment of geometry parameters, thereby boosting the structure performance to the limit. Geometry variable adjustment is often carried out using experience-driven parametric studies [1,2], which is inefficient for the majority of contemporary antenna systems. A recommended approach is the employment of rigorous numerical optimization. For reliability reasons, this is most often performed using full-wave electromagnetic (EM) simulation models [3]. The literature offers a plethora of optimization techniques, including local [4] (both gradient-based [5–7] and derivative free [8]), global [9–12], multi-criterial [13–15], but also specialized methods for uncertainty quantification (statistical analysis [16], robust design [17,18]). As the computational cost of EM-driven design is high, often prohibitive when using conventional methods [19], considerable research efforts have been directed towards acceleration. These include surrogate-assisted approaches involving both data-driven [20–25], and physics-based metamodels [26–29], machine learning frameworks [30–32], response feature technology [33,34], cognition-driven design [35], response correction techniques [36,37], but also variable-resolution methods [38,39].

While antenna performance enhancement through geometry parameter adjustment is by far the most widely used approach, it limits the number of potential options, especially in terms of the considered antenna topologies. The optimization process normally leads to a final design featuring an antenna type that is structurally similar to the initial one, with only different geometric dimensions. For example, when starting from an inverted-F antenna we usually end up with another inverted-F antenna [40]; a double T-shaped monopole normally leads to a slightly modified T-shaped monopole [41]. However, in many cases, restricting the optimization process to dimension adjustment of the fixed topology does not facilitate the exploration of other antenna topologies that may be more suitable for a given application and imposed size or other constraints. This is usually detrimental to the performance of other key features of the products, such as audio or a camera, as those components usually share a common PCB area with the antenna.

Alternative, and more generic approaches include topology optimization (TO) techniques. One of the possibilities is to discretize the space assigned to the antenna into a number of pixels (typically, rectangular cells) to construct a suitable topology, which is determined by either associating a given cell with metallization or leaving it empty [42–47]. While these methods enable considerable flexibility, the design problem typically turns into a combinatorial one. Also, controlling the topology resolution is not straightforward as changing the cell sizes alters the problem dimensionality. In some cases, only parts of the antenna topology (e.g., the radiator [42]) are discretized, which limits possible options. A slightly different methodology are pixel antennas, where the antenna topology is developed by (optimization-decided) connections between pre-defined metallic cells [48–51], or connections between freely moving patches [40]. The free-form TO methods exhibit improved flexibility due to nearly arbitrary parameterization of the antenna metallization [52–59]. Many of these techniques (e.g., [53,54]) incorporate fast custom EM FDTD solvers to expedite the optimization process. In the majority of the mentioned techniques, AI-based procedures (e.g., genetic/evolutionary algorithms) are employed to carry out the design process. In general, simultaneous optimization of antenna topology and its dimensions facilitates the generation of non-conventional structures with potentially at-

tractive features and competitive performance. This is particularly important from the perspective of today's industrial antenna design because it becomes increasingly more difficult to accommodate conventional types of antennas into highly integrated and highly functional portable devices.

This work proposes a novel approach to unsupervised specification-driven design of planar antennas. Its key component is a flexible parameterization of antenna geometry. It can be readily adjusted in terms of the complexity, thereby accommodating structures of different levels of topological sophistication. Furthermore, it facilitates both combinatorial and continuous optimization, which enables evolution of the antenna topology and, simultaneously, the adjustment of dimensions, all within the same parameterization framework. The antenna development is a two-stage process with the first stage realized as nature-inspired evolution of antenna geometry, and the second stage involving local (gradient-based) tuning of antenna dimensions. The same parameterization is employed throughout the entire design procedure. The presented framework operates entirely in a black-box fashion with no expert knowledge incorporated whatsoever. It has been demonstrated through the design of several dual- and triple-band but also broadband antennas under challenging scenarios (strict constraints on antenna footprint, the presence of environmental components). In all cases, novel and unconventional structures have been obtained that satisfy the prescribed performance requirements. At the same time, the computational costs of the design process are reasonable given unsupervised operation of the framework.

The technical contributions of this work can be summarized as follows: (i) development of a flexible and scalable parameterization of antenna structures, which is suitable for both combinatorial and continuous optimization, (ii) encapsulating tools for antenna topology alteration and dimension adjustment within the same parameterization described by a reasonably small number of variables, (iii) development of the algorithmic framework for unsupervised (specification-driven) antenna design, (iv) demonstrating practical utility of the framework using several examples of antennas designed under challenging scenarios (dual- and triple-band specifications, limited footprint, accounting for antenna environment). To the best knowledge of the authors, the presented methodology offers versatility and efficacy not reported so far in the literature.

2. Unsupervised Antenna Design: Methodology

This section introduces the proposed approach to unsupervised development of planar antennas. The keystone of our approach is a scalable antenna parameterization, which facilitates the generation and processing of complex geometries while maintaining reasonably low parameter space dimensionality. The latter is instrumental for efficient processing of antenna topologies and dimension sizing using numerical optimization techniques. The remainder of this section is organized as follows: Section 2.1 discusses the fundamental assumptions of the design process. Section 2.2 introduces antenna parameterization, whereas Section 2.3 outlines the computational model and the interface between programming environment (here, Matlab) and EM solver (here, CST Microwave Studio). Global and local optimization procedures are described in Sections 2.4 and 2.5, respectively, whereas Section 2.6 summarizes the entire design framework.

2.1. Prerequisites

In this work, the following assumptions are made about the antenna structures of interest:

- We consider single-layer microstrip antennas on rectangular-shape substrates;
- The ground plane is assumed to be rectangular, extending from the bottom of the substrate and along the entire substrate width. The ground plane height is determined by the optimization process;
- Front-side metallization structure is determined by the optimization process within the scope of the assumed parameterization (cf. Section 2.2);

- Excitation: a discrete port allocated at any point of the antenna; however, it should be over the ground plane and touching the front-side metallization.

The antenna structures generated using these guidelines cover a wide range of possible topologies.

2.2. Subsection

Antenna parameterization is developed based on the following prerequisites:

- Parameterization should provide sufficient flexibility to mimic the shapes of popular types of microstrip (monopoles, patch antennas, dipoles, etc.);
- It should contain continuous parameters (e.g., metallization patch sizes and location) to facilitate local tuning;
- It should contain discrete parameters to adjust the structure complexity;
- It should be scalable; in particular, parameterization that enables changing the number of antenna components, and, consequently, the number of adjustable parameters, is preferred over parameterizations featuring fixed numbers thereof;
- Parameterization should be easy to implement, handle, and extend in EM simulation environment (here, CST Microwave Studio).

A parameterization complying with the aforementioned prerequisites has been developed for the purpose of this work as described below. The antenna building blocks include the following (note: horizontal and vertical dimensions are marked using the subscript x and y, respectively):

- Substrate: It is assumed to be rectangular, of the size S_x and S_y (cf. Figure 1a). The substrate thickness is h, and its dielectric permittivity is ε_r (both may be fixed or variable, depending on designer's needs).
- Ground plane: A solid rectangle extending through the entire substrate in the x direction and l_g in the y direction (Figure 1b).
- Discrete port: The port location is p_x and p_y with respect to the center of a specified metallization patch, the port to the ground plane, and one of the metallization patches on the front side (cf. Figure 1c).
- Front-side metallic patches: The antenna contains N_P metallic patches, the centers of which can freely move within the substrate area. Each patch is parameterized using four parameters:
  - Center of the kth patch: $s_{x.k}$ (horizontal coordinate), $s_{y.k}$ (vertical coordinate);
  - Size of the kth patch: $h_{x.k}$ (horizontal coordinate), $h_{y.k}$ (vertical coordinate);

  for $k = 1, \ldots, N_P$. The patch center is allocated with respect to the center of the substrate (cf. Figure 2a). Further, the patches are trimmed as necessary to ensure that they do not extend beyond the substrate outline. Formally, patch trimming is realized using the following formulas (cf. Figure 2b):

$$h_{x.k} = \min(h_{x.k}, d_{x.k}), \quad \text{where } d_{x.k} = \frac{S_x}{2} - |s_{x.k}| \tag{1}$$

$$h_{y.k} = \min(h_{y.k}, d_{y.k}), \quad \text{where } d_{y.k} = \frac{S_y}{2} - |s_{y.k}| \tag{2}$$

The patches are concatenated in a Boolean sense to form the front metallization of the antenna structure.

- Front-side holes: The antenna may contain N_H holes, which are understood as the areas with removed metallization. As for the patches, the centers of the hole can move freely. Each hole is parameterized using four parameters:
  - Center of the kth hole: $s_{hx.k}$ (horizontal coordinate), $s_{hy.k}$ (vertical coordinate);
  - Size of the kth hole: $h_{hx.k}$ (horizontal coordinate), $h_{hy.k}$ (vertical coordinate);

For $k = 1, \ldots, N_H$. The hole center is allocated with respect to the center of the substrate (cf. Figure 3a). The holes are subtracted from front-side metallization in a Boolean sense, as shown in Figure 3.

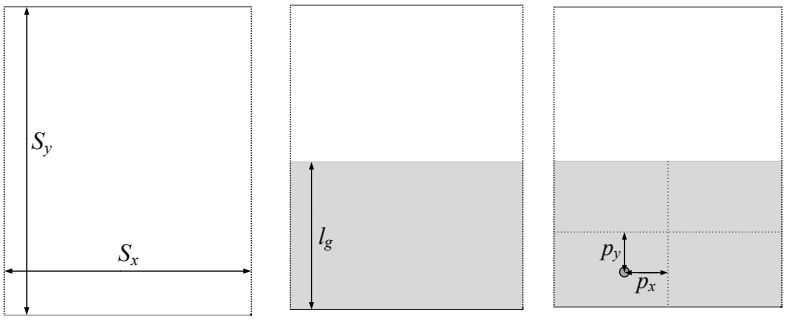

Figure 1. Elementary structural components of antenna parameterization and their dimensional variables: (**a**) substrate, (**b**) ground plane, (**c**) discrete port.

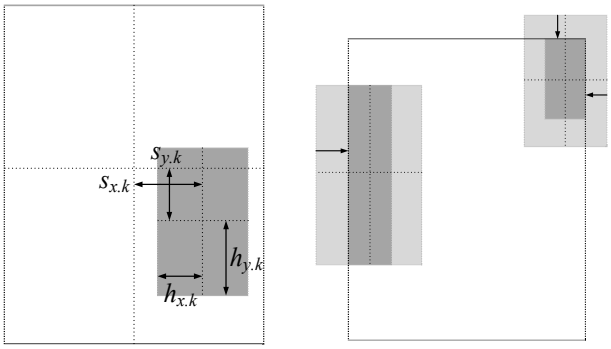

Figure 2. Front-side metallic patches: (**a**) parameterization; (**b**) trimming process, where light- and dark-grey shade represents the original and trimmed patches, respectively.

All antenna parameters, including dimensions of the substrate, port location, location and sizes of the patches and holes are gathered into a parameter vector $\boldsymbol{x}$ to be processed by the optimization algorithms, both global and local.

The proposed parameterization allows for rendering a plethora of conventional antenna geometries, some of which are shown in Figure 4, see also Figure 5. The shown topologies are just examples; in practice, the antenna shapes produced by the optimization algorithm are to be irregular, unlike those obtained using the engineering insight. Due to continuously adjusted sizes of metallic patches and holes, the resolution of antenna geometry can be globally and locally altered without the necessity of introducing any additional components. The same can be said about the overall antenna size as well as the overall complexity of the structure. In particular, the number of building blocks can be modified during the design process while maintaining fixed dimensionality of the parameter space. Further, the parameter space dimensionality can be readily adjusted in a linear fashion by adding the number of geometry components, which is in contrast to mesh-type of parameterization, where even small changes in the mesh density have profound effects on the effective number of design variables. Because of being primarily based on continuous variables, the proposed parameterization is suitable to work with local (both gradient-based and stencil-based) optimization algorithms. The proposed parameterization addresses a number of common issues pertinent to unit-cell based approaches (also referred to as pixel-based antennas and similar), which exhibit several serious issues: (i) limited number of antenna topologies, which are confined to the location of the unit cells; (ii) limited resolution of establishing antenna dimensions (also confined to the unit cell size); (iii) considerably larger dimensionality of parameter space, which leads to

numerical problems, in particular, longer and therefore more expensive optimization runs; (iv) it is not possible to use gradient-based optimization routines, as antenna design tasks are of combinatorial nature.

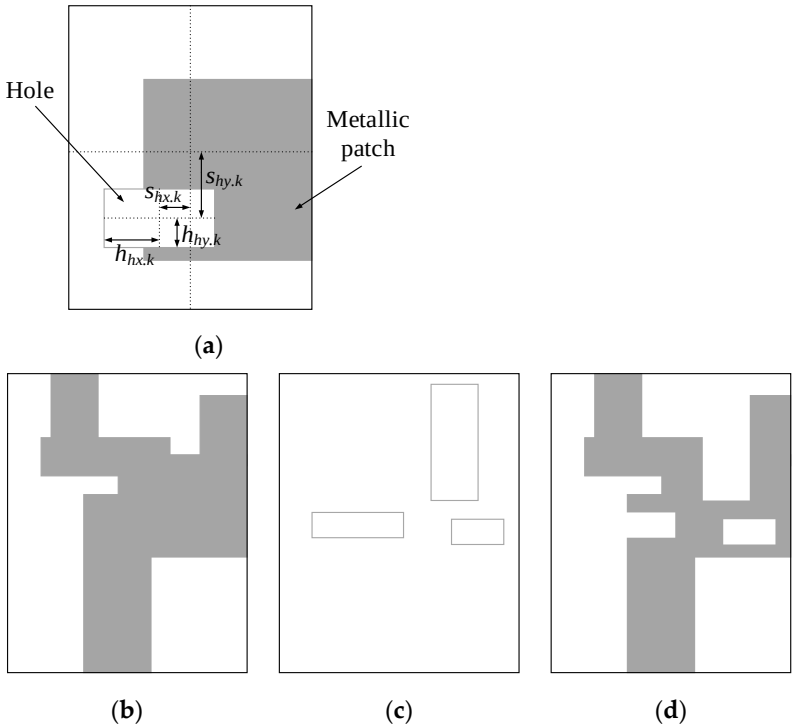

Figure 3. Incorporation of holes as constituting components of antenna structure: (**a**) hole size and positioning. Examples of concatenating the building blocks to form the antenna geometry: (**b**) initial metallization (concatenated patches), (**c**) hole location, and (**d**) final metallization upon Boolean subtraction of the holes.

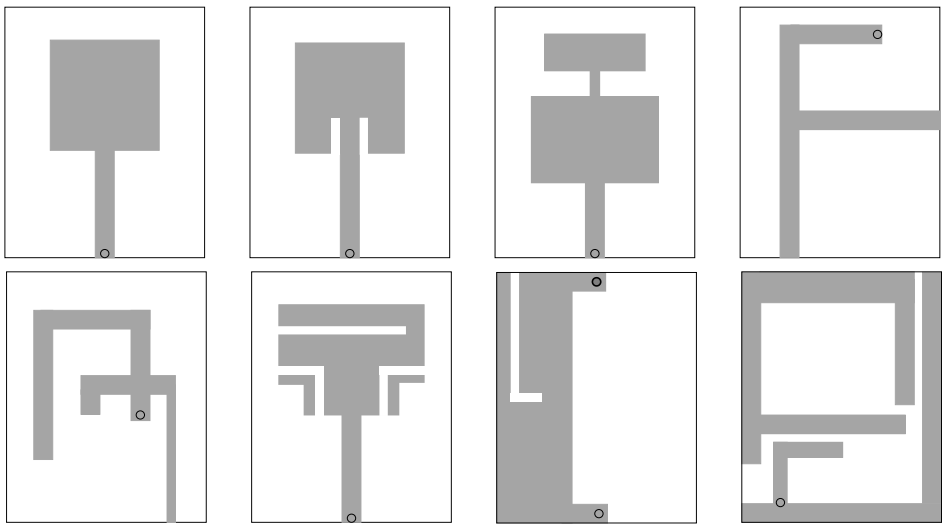

Figure 4. Examples of various conventional geometries that can be mimicked using the proposed antenna parameterization.

2.3. Computational Model

In this work, the computational model is realized in CST Microwave Studio [60]. The raw model, shown in Figure 6 implements sixteen front-side patches and eight holes, which represent the maximum complexity (N_P = 16, N_H = 8), more than sufficient for practical applications.

While evaluating the antenna responses, the vector of geometry parameters (cf. Section 2.2) is transformed into actual (absolute) locations and sizes of the antenna building blocks. The patches and holes whose indices exceed N_P and H_N, respectively, are removed from the model by assigning zero sizes to those components. This provides convenient control over the model's complexity. As mentioned earlier, the patch/hole sizes are relative to the size of the substrate. The lower and upper bounds on these sizes may be assigned as zero and one, respectively.

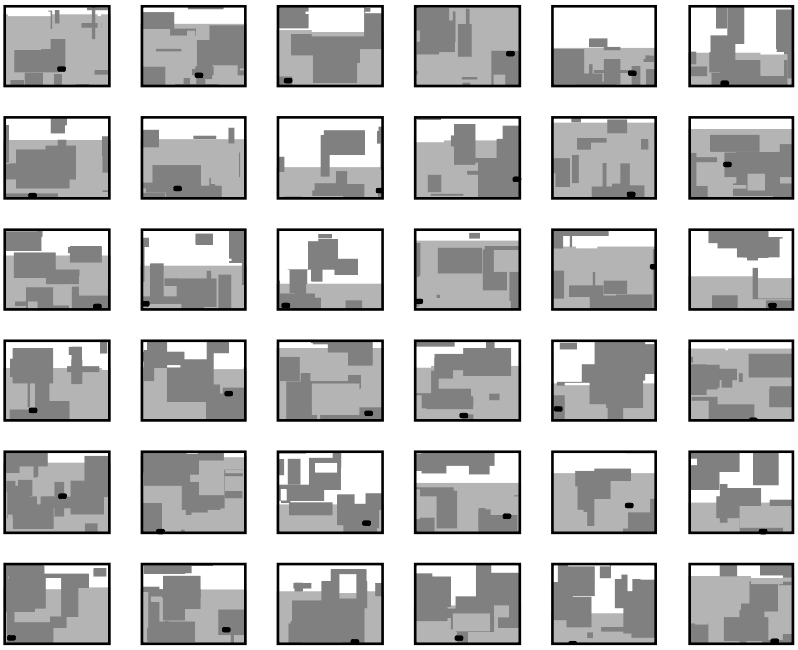

Figure 5. Random antenna geometries generated assuming $N_P = 12$ and $N_H = 2$, shown to demonstrate flexibility of the presented parameterization. Light-grey shade marks the ground plane; black circle represents a discrete port.

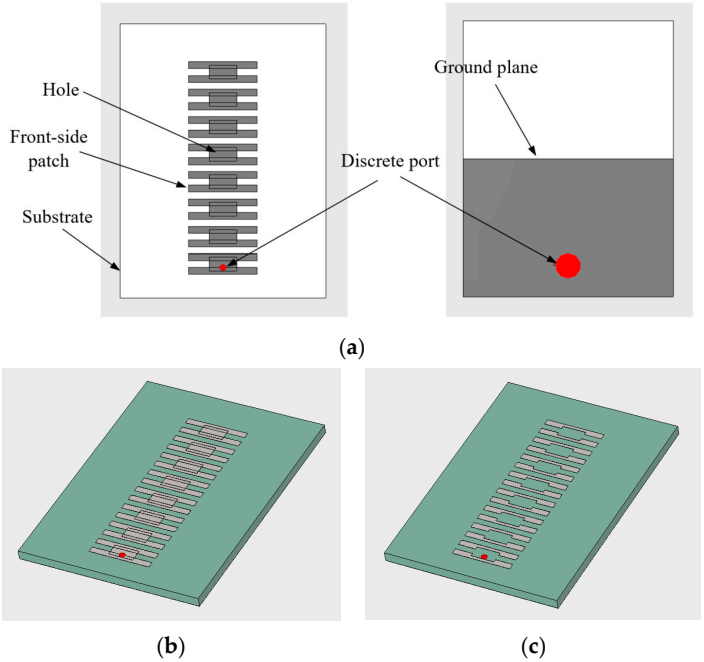

Figure 6. Raw computational model (here, implemented in CST Microwave Studio): (**a**) model structure (front view—left; back view—right) assuming maximum complexity of sixteen patches and eight holes; (**b**) 3D view of the raw model; (**c**) 3D view of the raw model after applying Boolean transformation on the front-side metallization.

Model evaluation is realized using the interface between the programming environment (here, Matlab) and the EM solver, which has been outlined in Figure 7. The critical component thereof is a Visual Basic script synthesized to adjust the parameter values and simulation setup variables, based on the input parameters supplied to the interface.

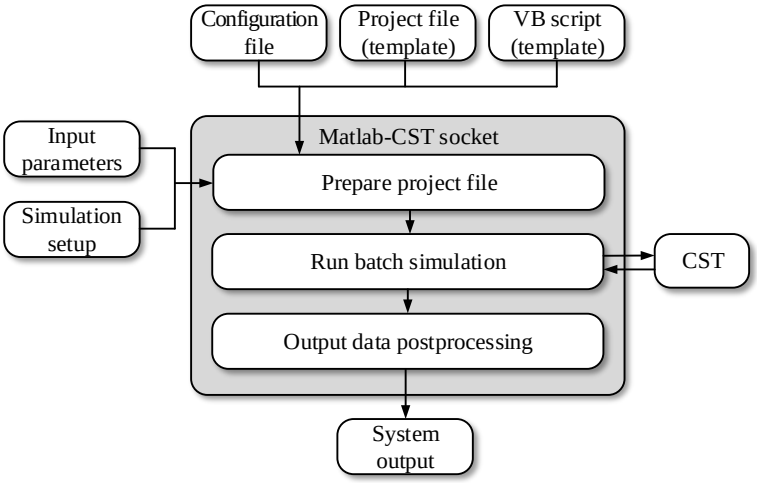

Figure 7. Interfacing programming environment and EM solver. Based on the input parameters (antenna geometry) and simulation parameters, a temporary project file is rendered using the templates associated with the model (here, the .cst project file and Visual Basic script). Batch-mode antenna evaluation is followed by post-processing of the exported simulation data.

Antenna evaluation is carried out by transforming the raw model into a specific antenna architecture (based on the input parameters), conducting batch-model simulation, and post-processing the results. Figure 8 provides an illustration example.

Figure 8. Evaluation example of the computational model: (**a**) raw model, (**b**) model transformed into a specific antenna structure using parameterization of Section 2.2, (**c**) antenna response (here, the reflection characteristic) obtained through batch-model simulation realized using the socked of Figure 7.

2.4. Design Problem Formulation. Global Optimization

Figure 9 presents the flow diagram of the design process, which is pertinent to both global search outlined in this section, and local tuning (cf. Section 2.5). The process is entirely specification driven with the only input provided by the user being design specifications, and supplementary data (e.g., substrate parameters, design constraints such as the maximum allowed antenna size, etc.). In this work, design specifications are formulated for antenna reflection characteristics. Given the target operating frequency bands $[f_{1.1}\ f_{1.2}]$, ..., $[f_{K.1}\ f_{K.2}]$, where K is the number of bands, the objective is to find antenna geometry for which the maximum in-band reflection level does not exceed −10 dB. Formally, the problem is formulated as

$$\boldsymbol{x}^* = \arg\min_{\boldsymbol{x}\in X} U(\boldsymbol{x}) \tag{3}$$

where $\boldsymbol{x}^*$ is the optimum design to be identified (recall that $\boldsymbol{x}$ is a vector of all adjustable parameters), X is the parameter space determined by the lower/upper bounds on the antenna variables, and U is the minimax objective function defined as

$$U(\boldsymbol{x}) = \max_{f \in F} \{|S_{11}(\boldsymbol{x}, f)|\} \tag{4}$$

where $F = [f_{1.1}\, f_{1.2}] \cup [f_{2.1}\, f_{2.2}] \cup \ldots \cup [f_{K.1}\, f_{K.2}]$ ($\cup$ denotes the set-theory summation).

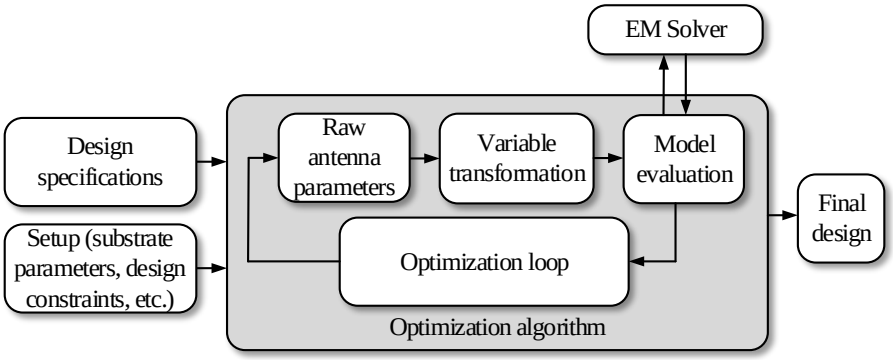

Figure 9. Flow diagram of unsupervised antenna development using optimization tools and parameterization of Section 2.2.

It should be emphasized that one of the fundamental advantages of the parameterization introduced for the purpose of this work is that the vector $\boldsymbol{x}$ determines—at the same time—the antenna topology and specific dimensions. This means that the same set of parameters can be processed using global search methods (to determine the optimum antenna topology) and local algorithms (to fine-tune the antenna performance).

The core algorithmic tool employed to perform antenna structure development using the parameterization of Section 2.2 is a floating-point evolutionary algorithm with elitism and adaptive adjustment of the mutation rate. The algorithm is similar to standard evolutionary procedures (see, e.g., [61]). The main components of the algorithm include the following:

- Generational model (a new population entirely replaces the previous one). The population size N is set to 20;
- Binary tournament selection [62];
- Elitism scheme with a single best individual inserted to the next population (with by-passing recombination operators);
- A mixture of intermediate and arithmetic crossover (with equal probabilities). Let $\boldsymbol{x} = [x_1 \ldots x_n]^T$ and $\boldsymbol{y} = [y_1 \ldots y_n]^T$ be the parent individuals, and $\boldsymbol{z} = [z_1 \ldots z_n]^T$ be an offspring. The intermediate crossover produces $\boldsymbol{z}$ so that $z_i = ax_i + (1 - a)y_i$ with $0 \leq a \leq 1$ (a selected randomly); the arithmetic crossover yield $\boldsymbol{z} = a\boldsymbol{x} + (1 - a)\boldsymbol{y}$ with $0 \leq a \leq 1$ (a selected randomly). The crossover probability is $p_m = 0.8$;
- Random mutation with non-uniform probability distribution. It is applied individually to each parameter vector component so that $x_i \rightarrow x_i' = x_i + \Delta x_i$, where Δx_i is a random deviation defined as

$$\Delta x_i = \begin{cases} (x_{i.\max} - x_i) \cdot (2(r - 0.5))^{\beta} & \text{if } r > 0.5 \\ (x_{i.\min} - x_i) \cdot (2(0.5 - r))^{\beta} & \text{otherwise} \end{cases} \tag{5}$$

  where $r \in [0, 1]$ is a random number and $\beta = 3$;
- Termination based on exceeding computational budget (the maximum number of iterations denoted as N_i).

Furthermore, adaptive adjustment of mutation rate p_m is implemented as follows. Let P_D be a population diversity defined as

$$P_D = \frac{1}{n}\sum_{k=1}^{n} std([x_{1.k}\ x_{2.k}\ \ldots\ x_{N.k}]) \tag{6}$$

where $\boldsymbol{x}^j = [x_{j.1} \ldots x_{j.n}]^T$ is jth member of the population, and $x_{j.k}$ is its kth entry. Thus, P_D is the average standard deviation of the population averaged over all antenna parameters. The mutation rate ${p_m}^{(i+1)}$ for iteration i of the algorithm is determined as follows (the initial mutation rate ${p_m}^{(0)}$ is set to 0.2):

if $i < N_i/2$

if $P_D < P_{D\min}$

${p_m}^{(i+1)} = {p_m}^{(i)} m_{incr}$

elseif $P_D > P_{D\max}$

${p_m}^{(i+1)} = {p_m}^{(i)} / m_{decr}$

end

else

$$p_m^{(i+1)} = p_m^{(N_i/2)} \left(\frac{2(N_i - i)}{N_i}\right)^2 \tag{7}$$

end

Here, we use $P_{D\min} = 0.05$, $P_{D\max} = 0.1$, $m_{incr} = 1.3$, and $m_{decr} = 1.2$. The multiplication factors are not critical due to self-adjustment. The minimum/maximum population diversities are set having in mind that most of antenna parameters are relative (i.e., change between zero and one). In the second half of the search process, mutation probability gradually decreases to zero, which improves exploitation capability of the algorithm. The flow diagram of the evolutionary algorithm can be found in Figure 10.

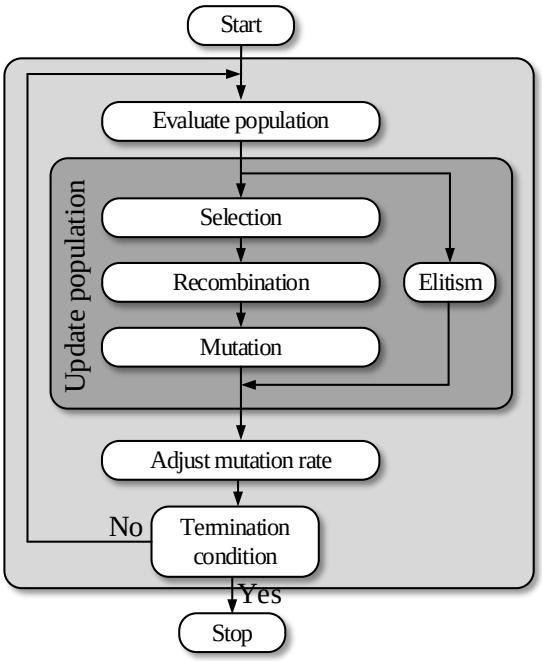

Figure 10. Flow diagram of evolutionary algorithm with elitism and adaptive adjustment of mutation rate.

2.5. Local Parameter Tuning

The purpose of the second optimization stage is to improve antenna performance (here, impedance matching over the target operating bands) through local tuning of an-

tenna parameters. In this work, we use a trust-region gradient-based algorithm [63] with numerical derivatives [64], which is briefly outlined below.

The goal is to again solve the problem (3), (4); however, the starting point is the design obtained through global search (cf. Section 2.4), which will be denoted as $\boldsymbol{x}^{(0)}$. The algorithm produces a series of approximations $\boldsymbol{x}^{(i)}$, $i = 0, 1, \ldots$, of approximations to the optimum design $\boldsymbol{x}^*$ using a linear (first-order Taylor) model of antenna responses established at the current iteration point. The details of the algorithm can be found in Algorithm 1. The problem (9) is solved using Sequential Quadratic Approximation (SQP) algorithm [65] implemented as a part of the Matlab Optimization Toolbox [66].

Algorithm 1. The outline of trust-region gradient-based algorithm with numerical derivatives

Optimization problem (cf. (1), (2)):

$$\boldsymbol{x}^* = \arg\min_{\boldsymbol{x} \in X} U(\boldsymbol{x}) \tag{8}$$

Algorithm operation: the TR algorithm generates a sequence $\boldsymbol{x}^{(i)}$, $i = 0, 1, 2, \ldots$ as

$$\boldsymbol{x}^{(i+1)} = \arg\min_{\boldsymbol{x};\ ||\boldsymbol{x}-\boldsymbol{x}^{(i)}|| \le d^{(i)}} U_L(\boldsymbol{x}) \tag{9}$$

Objective function U_L: is defined as in (4) but with the antenna response S_{11} evaluated using its first-order Taylor model:

$$S_{11L}^{(i)}(\boldsymbol{x}, f) = S_{11L}^{(i)}(\boldsymbol{x}^{(i)}, f) + \boldsymbol{G}_{11}(\boldsymbol{x}^{(i)}, f) \cdot (\boldsymbol{x} - \boldsymbol{x}^{(i)}) \tag{10}$$

In (10), $\boldsymbol{G}_{11}(\boldsymbol{x},f)$ is the gradient of $S_{11}(\boldsymbol{x},f)$ at $\boldsymbol{x}$ and frequency f evaluated using finite differentiation [63].
Gain ratio r: EM-evaluated versus linear-model predicted objective function improvement

$$r = \frac{U(\boldsymbol{x}^{(i+1)}) - U(\boldsymbol{x}^{(i)})}{U_L(\boldsymbol{x}^{(i+1)}) - U_L(\boldsymbol{x}^{(i)})} \tag{11}$$

Trust region size $d^{(i)} > 0$: adaptively adjusted based on r; $d^{(i+1)} = d^{(i)} m_{incr}$ if $r > r_{incr}$, and $d^{(i+1)} = d^{(i)} / m_{decr}$ if $r < r_{decr}$; standard control parameter values are $r_{incr} = 0.75$, $r_{decr} = 0.25$, $m_{incr} = 1.5$, $m_{decr} = 2$ [67].
Acceptance of the new iteration point: $\boldsymbol{x}^{(i+1)}$ is accepted only if $r > 0$ (i.e., EM-evaluated objective function improvement has been observed); otherwise, the iteration is repeated with reduced TR size;
Algorithm termination: convergence in argument ($||\boldsymbol{x}^{(i+1)} - \boldsymbol{x}^{(i)}|| < \varepsilon$) or sufficient reduction of the TR size ($d^{(i)} \le \varepsilon$); the termination threshold is set to $\varepsilon = 10^{-3}$.

It should be noted that each iteration of the algorithm requires at least $n + 1$ EM analyses (n being the parameter space dimensionality). In our implementation, the finite-differentiation-based sensitivity estimation is also used for parameter pre-screening. The parameters for which sensitivity is zero (e.g., due to a particular antenna building block being inactive) are excluded from the optimization process, which reduces the overall cost.

It should be reiterated that due to the assumed antenna parameterization, the same parameter vector $\boldsymbol{x}$ can be employed to realize both the global and local search stage. This is because large-scale adjustments of these parameters directly affect the antenna topology, whereas localized changes only alter antenna responses while keeping the topology intact.

2.6. Complete Design Framework

Figure 11 shows the flow diagram of the proposed framework for unsupervised design of planar antennas. The process is specification driven and unsupervised in the sense that both antenna topology and its specific dimensions are automatically generated using a two-stage optimization process as described in Sections 2.4 and 2.5. The only input information provided by the user are design specifications on antenna reflection (cf. (4)), as

well as additional requirements (e.g., material parameters of the substrate the antenna is to be implemented on, substrate dimensions or constraints on maximum antenna footprint area, etc.). As of now, parameterization complexity, i.e., the numbers N_P and N_H of active components (patches and holes) is decided upon beforehand.

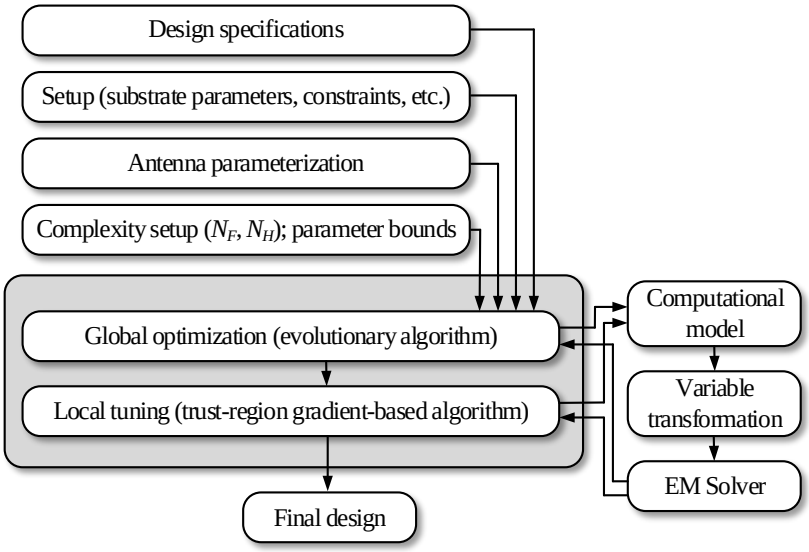

Figure 11. Flow diagram of the unsupervised antenna design framework proposed in this work.

3. Demonstration Examples

This section provides several illustration examples demonstrating the operation of the proposed unsupervised antenna design system. These are described in Sections 3.1–3.6. Section 3.7 summarizes the results and the system performance.

3.1. Case I

The first example is a dual-band antenna implemented on FR-4 substrate (ε_r = 4.4, h = 1 mm). The antenna size is predefined to 30 × 6 mm. The ground plane is recessed by 5 mm, and the structure is surrounded by a metallic environment (modeled as perfectly electrical conductor), as shown in Figure 12. The design specifications imposed on antenna reflection are as follows: $|S_{11}(\boldsymbol{x},f)| \leq -10$ dB for $2.40 \leq f \leq 2.48$ GHz, and $5.1 \leq f \leq 5.9$ GHz.

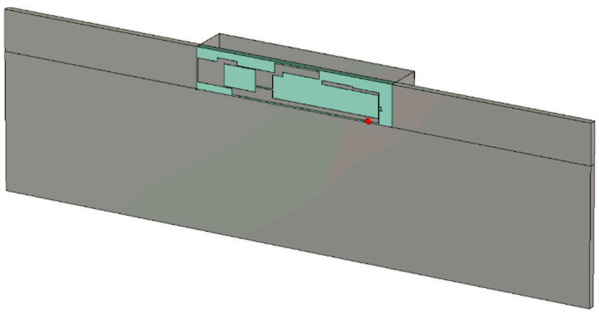

Figure 12. Illustration case I: dual-band antenna with recessed ground plane.

The antenna has been designed using the approach of Section 2, with N_P = 4 and N_H = 7. Figure 13 shows selected snapshots of the global search stage, where the computational budget of the evolutionary algorithm was set to 2000 (population size of 10, maximum iteration count of 100). The antenna geometry obtained upon the conclusion of the global search stage and its reflection characteristic has been shown in Figure 14. The local tuning only takes six iterations, as shown in Figure 15. At the final design, design specifications are satisfied, with $|S_{11}|$ being below −10 dB across both operating bands.

Figure 16 shows the realized gain and total efficiency. The maximum gain is about 4.4 dB and 4.3 dB in the lower and upper band, respectively, whereas the efficiency reaches about 96% in the lower band with the average in-band efficiency in the upper band being around 97%. These numbers indicate that the antenna performance is satisfactory, especially given the size constraints. Radiation patterns in the *yz*- and *xz*-plane have been shown in Figure 17. The characteristics are close to omnidirectional, which is preferred given the intended application of the structure (smart glasses). Finally, Figure 18 shows the surface current distribution at the three antenna resonances. It can be observed that the geometrical components of the architecture the antenna evolved into are quite 'economically' re-used at various parts of the operating spectrum. Again, it should be reiterated that the design process has been purely specification driven and unsupervised.

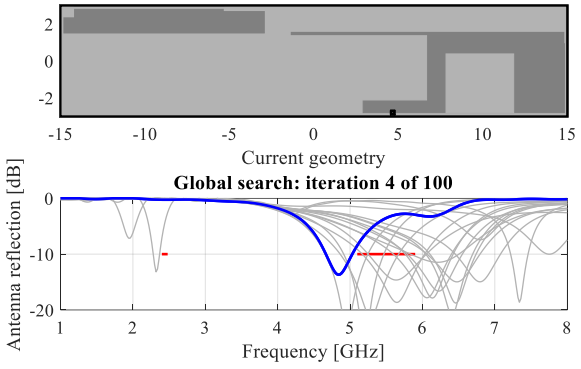

(**a**)

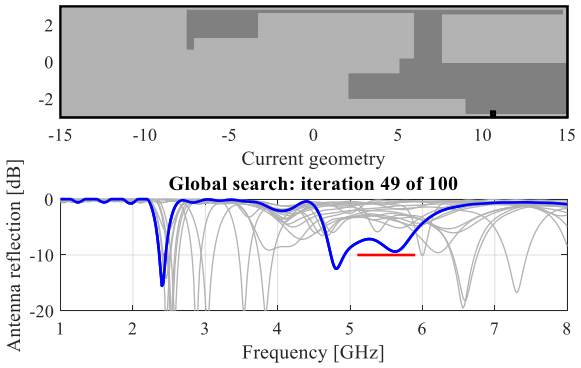

(**b**)

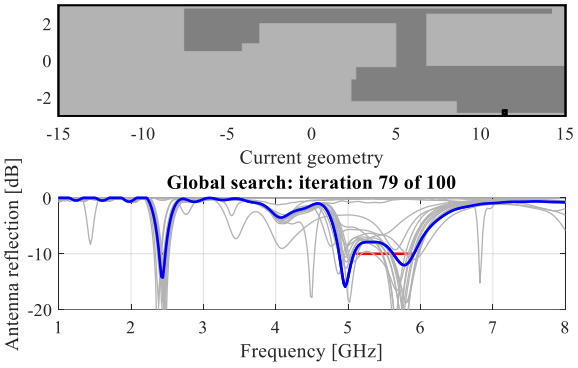

(**c**)

Figure 13. Global optimization stage: antenna geometry and reflection responses at selected algorithm iterations. Thick line represents the best response found so far, whereas thin lines stand for the responses corresponding to the current population processed by the algorithm. Design specifications marked using horizontal lines: (**a**) iteration 4, (**b**) iteration 50, and (**c**) iteration 80.

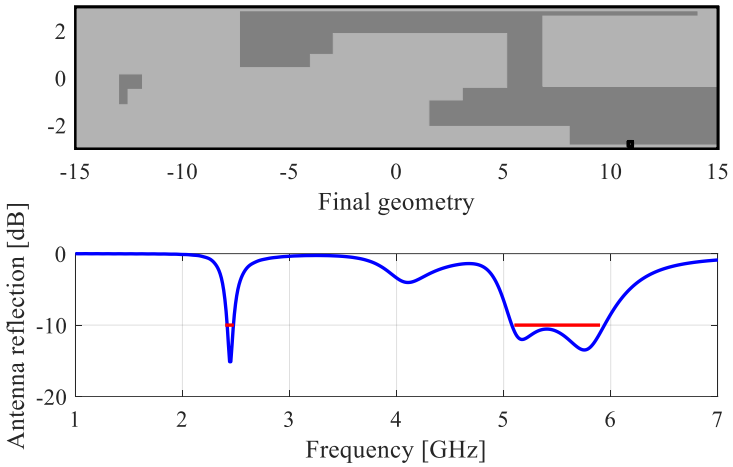

Figure 14. Antenna geometry and the reflection response upon termination of the global search stage. Port location marked as the black circle. Horizontal lines mark target operating bands.

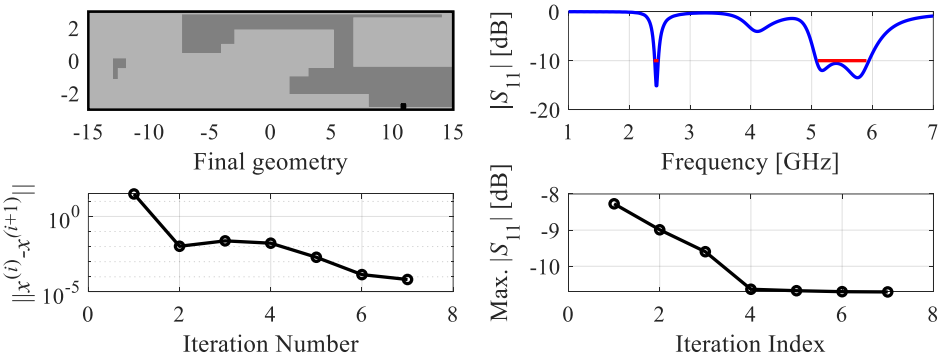

Figure 15. Final antenna geometry and reflection response upon conclusion of the local parameter tuning. The bottom pictures show the convergence plot and the evolution of the minimax objective function (2), respectively. Horizontal lines mark target operating bands.

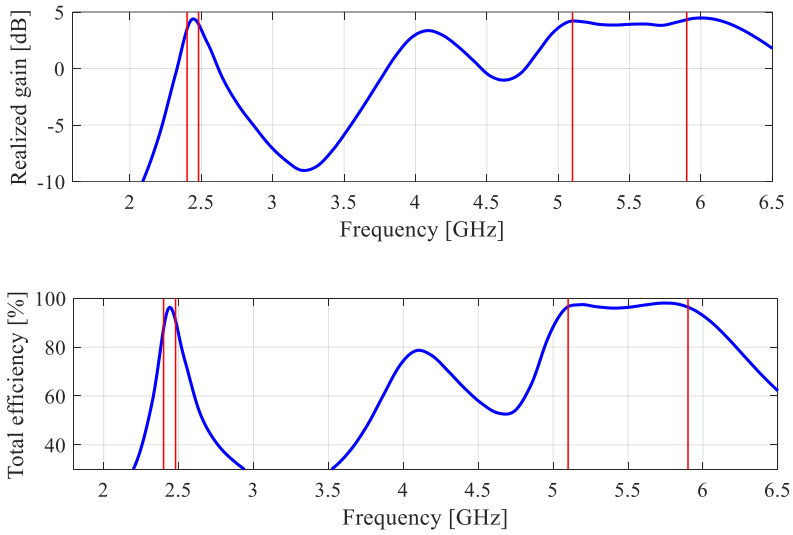

Figure 16. Realized gain and total efficiency of the antenna of Figure 15. Vertical lines mark the operating bands.

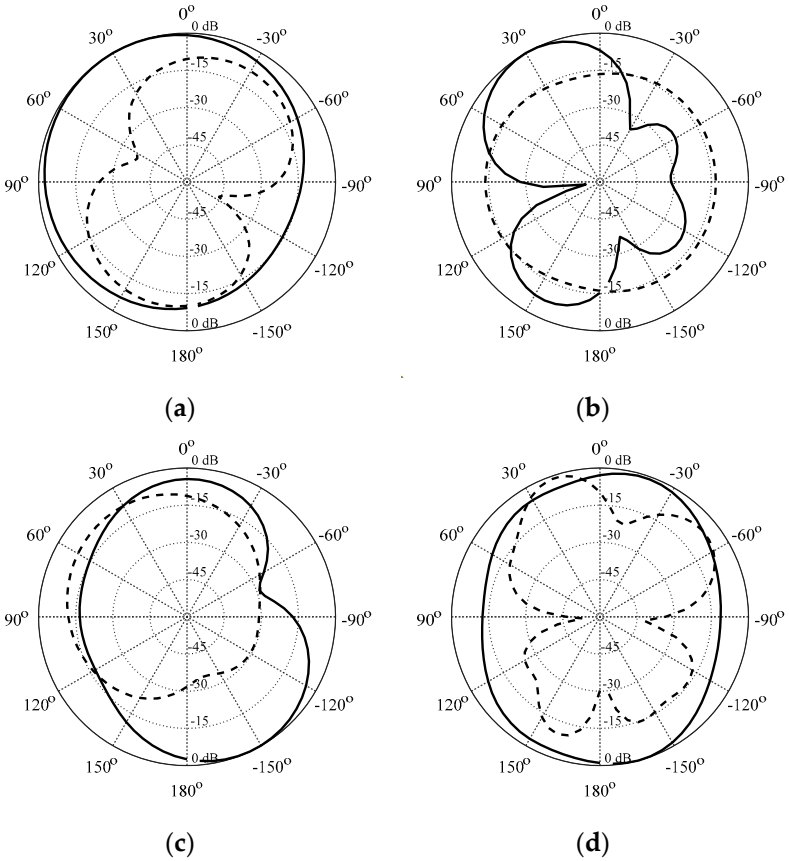

Figure 17. Radiation patterns (normalized directivity): (**a**) 2.45 GHz, *yz*-plane, (**b**) 2.45 GHz, *xz*-plane, (**c**) 5.5 GHz, *yz*-plane, and (**d**) 5.5 GHz, *xz*-plane. Co-pol and cross-pol patterns shown using the solid and dashed lines, respectively.

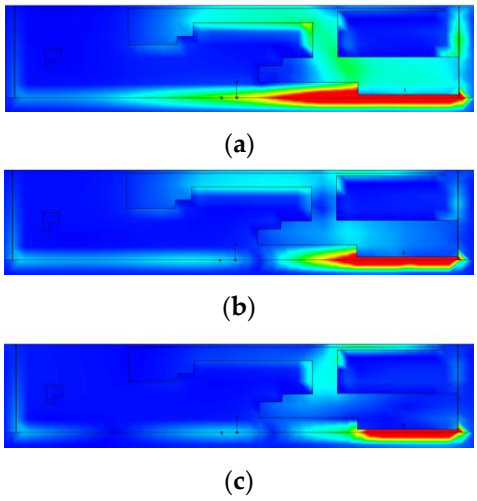

Figure 18. Surface current distributions at antenna resonances: (**a**) 2.45 GHz, (**b**) 5.16 GHz, and (**c**) 5.75 GHz.

3.2. Case II

The second case study is also a dual-band antenna implemented on FR-4 substrate ($\varepsilon_r = 4.4$, $h = 1$ mm). The antenna size is the same as for Case I, i.e., 30 × 6 mm. The computational model contains the same metallic environment; however, there is no recessed ground plane (cf. Figure 19). The design specifications imposed on antenna reflection are $|S_{11}(\boldsymbol{x},f)| \leq -10$ dB for $2.40 \leq f \leq 2.48$ GHz, and $5.0 \leq f \leq 7.0$ GHz.

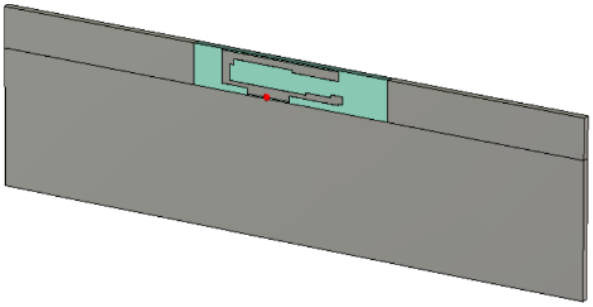

Figure 19. Illustration case II: dual-band antenna without recessed ground plane.

The antenna has been designed using the framework of Section 2 under an identical setup. Figure 20 shows the final geometry along with the reflection characteristic. The −10 dB impedance bandwidth is from 2.40 GHz to 2.49 GHz (lower band) and from 4.89 GHz to 7.14 GHz (upper band), which is more than is required according to specifications. It should be noted that the geometry is entirely different than for Case I. Figures 21 and 22 show realized gain, total efficiency, and radiation patterns, respectively. The gain is 2.8 dB and 4.2 dB in the lower and upper band, respectively, whereas the efficiency reaches 92% at the lower band, and the average of 98% in the upper band. Radiation characteristics are close to omnidirectional in the *yz*-plane.

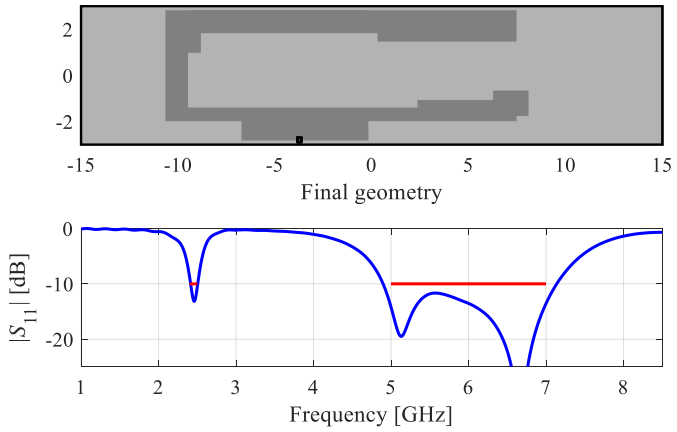

Figure 20. Case II: final antenna geometry and the reflection response. Port location marked as the black circle. Horizontal lines mark target operating bands.

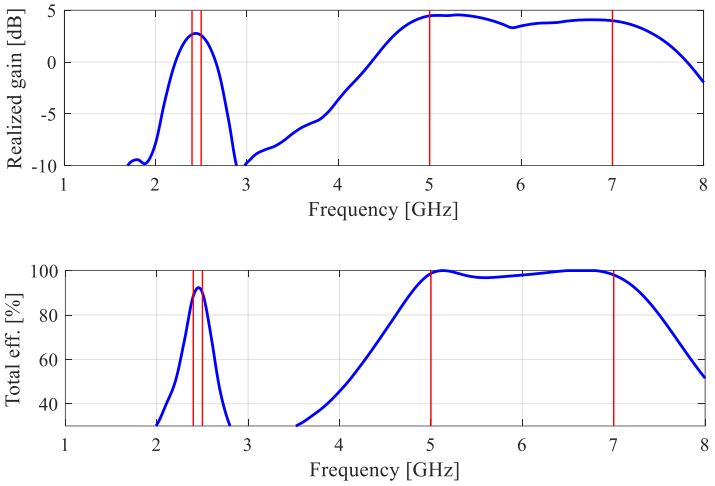

Figure 21. Realized gain and total efficiency of the antenna of Figure 20. Vertical lines mark the operating bands.

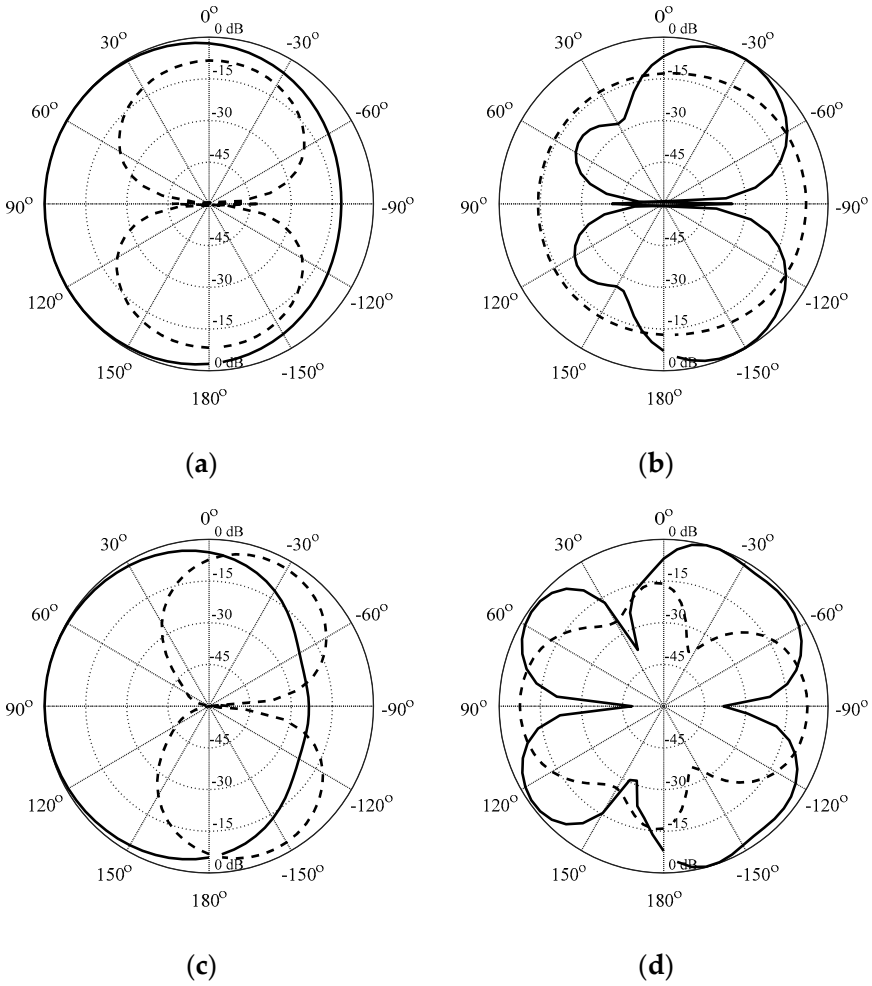

Figure 22. Radiation patterns (normalized directivity): (**a**) 2.45 GHz, *yz*-plane, (**b**) 2.45 GHz, *xz*-plane, (**c**) 6.0 GHz, *yz*-plane, and (**d**) 6.0 GHz, *xz*-plane. Co-pol and cross-pol patterns shown using the solid and dashed lines, respectively.

3.3. Case III

Our third example is a triple-band antenna implemented on 1.5 mm thick FR-4 substrate ($\varepsilon_r = 4.4$). The antenna size is 40 × 12 mm (see Figure 23). The design specifications are $|S_{11}(\boldsymbol{x},f)| \leq -10$ dB for $2.40 \leq f \leq 2.48$ GHz, $5.15 \leq f \leq 7.13$ GHz, $7.75 \leq f \leq 8.25$ GHz. The framework of Section 2 has been used to design the antenna using the same setup as for the previous examples. Figures 24–26 show the reflection characteristic, realized gain, total efficiency, as well as radiation patterns at 2.45 GHz, 6.15 GHz, and 8.0 GHz (centers of the respective operating bands).

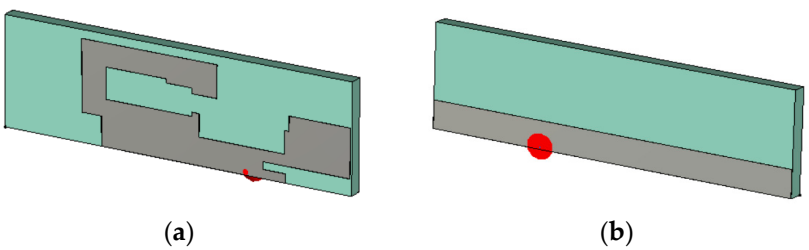

Figure 23. Illustration case III: 40 × 12 mm triple-band antenna: (**a**) front view; (**b**) back view.

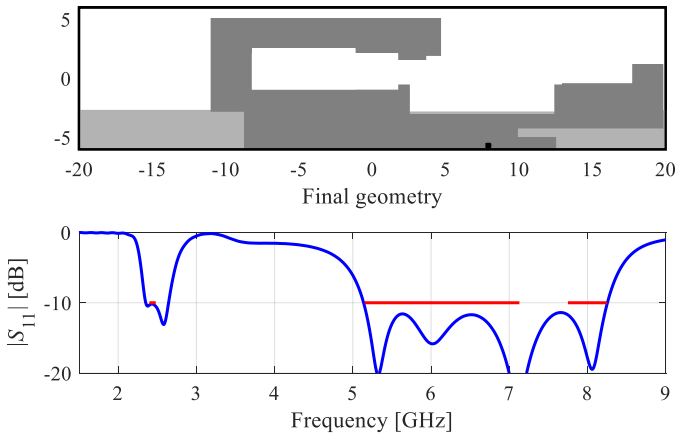

Figure 24. Case III: final antenna geometry (not in the right proportions) and the reflection response. Port location marked as the black circle. Light-gray shade marks the antenna ground. Horizontal lines mark target operating bands.

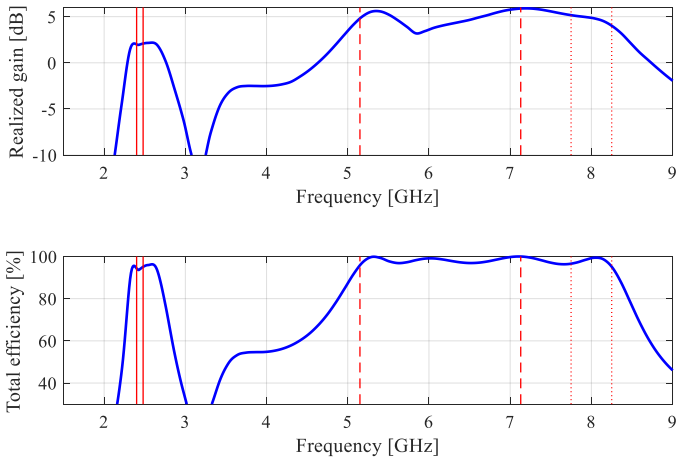

Figure 25. Realized gain and total efficiency of the antenna of Figure 24. Vertical lines mark the operating bands.

3.4. Case IV

The next example is a compact ultra-wideband antenna, also implemented on 1.5 mm thick FR-4 substrate (ε_r = 4.4). The antenna size is 25 × 15 mm, as shown in Figure 27. The design specifications are $|S_{11}(\boldsymbol{x},f)| \leq -10$ dB for $3.1 \leq f \leq 10.6$ GHz. As before, the framework of Section 2 has been used to design the antenna using the same setup as for the previous examples. Figures 28–30 show the reflection characteristic, radiation patterns at 4 GHz, 6 GHz, and 8 GHz, as well as realized gain and total efficiency. Note that there is a slight violation of the at the lower end of the operating band (about 0.5 dB).

3.5. Case V

The fifth example is a triple-band antenna realized on 1.5 mm thick FR-4 substrate (ε_r = 4.4). The antenna size is 50 × 20 mm, cf. see Figure 31. The design specifications are $|S_{11}(\boldsymbol{x},f)| \leq -10$ dB for $1.57 \leq f \leq 1.58$ GHz, $2.40 \leq f \leq 2.48$ GHz, and $5.15 \leq f \leq 5.85$ GHz. The antenna can be considered compact given that it is supposed to include the GSM band (1.57 GHz to 1.58 GHz). The design obtained using the proposed framework has been shown in Figure 32. The realized gain and total efficiency responses, as well as radiation patterns, can be found in Figures 33 and 34, respectively. As it can be observed, despite its compact size, the antenna is well matched within all prescribed operating bands; as a matter of fact, the actual −10 dB bandwidths are considerably wider than the assumed targets.

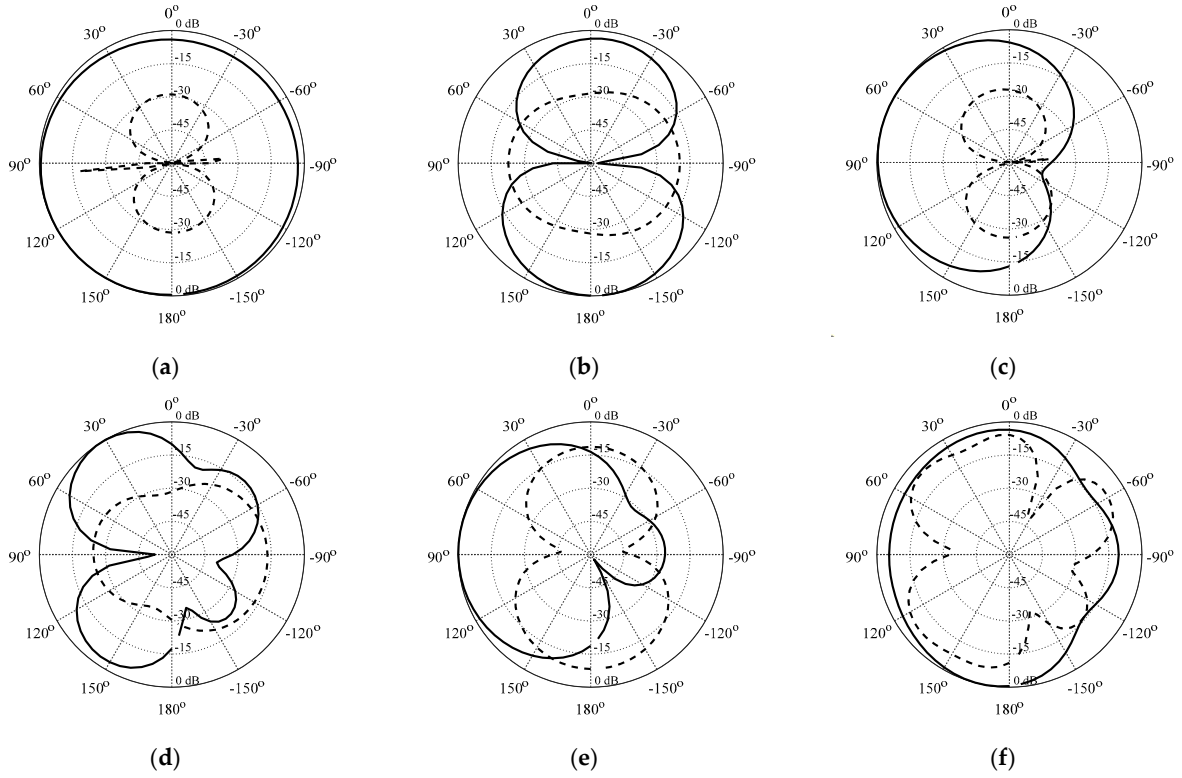

Figure 26. Radiation patterns (normalized directivity): (**a**) 2.45 GHz, *yz*-plane, (**b**) 2.45 GHz, *xz*-plane, (**c**) 6.15 GHz, *yz*-plane, (**d**) 6.15 GHz, *xz*-plane, (**e**) 8.0 GHz, *yz*-plane, and (**f**) 8.0 GHz, *xz*-plane. Co-pol and cross-pol patterns shown using the solid and dashed lines, respectively.

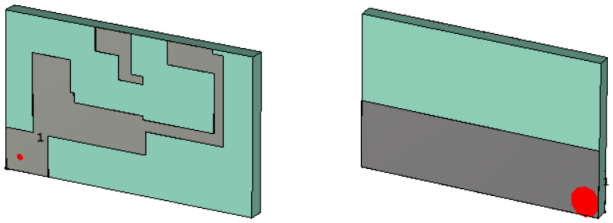

Figure 27. Illustration case IV: 25 × 15 mm ultra-wideband antenna: (**a**) front view; (**b**) back view.

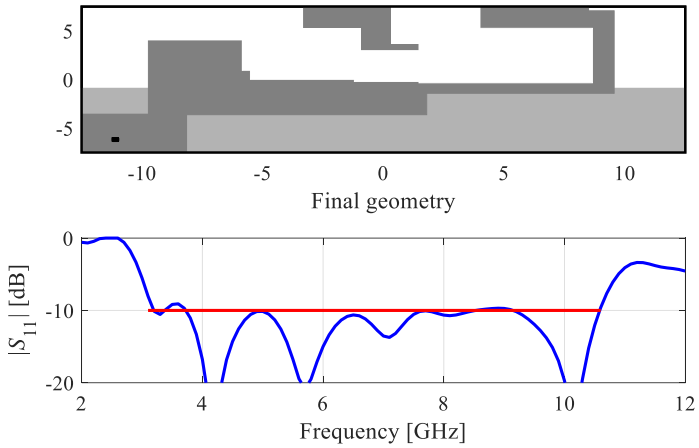

Figure 28. Case IV: final antenna geometry (not in the right proportions) and the reflection response. Port location marked as the black circle. Light-gray shade marks the antenna ground. The horizontal line marks the target operating band.

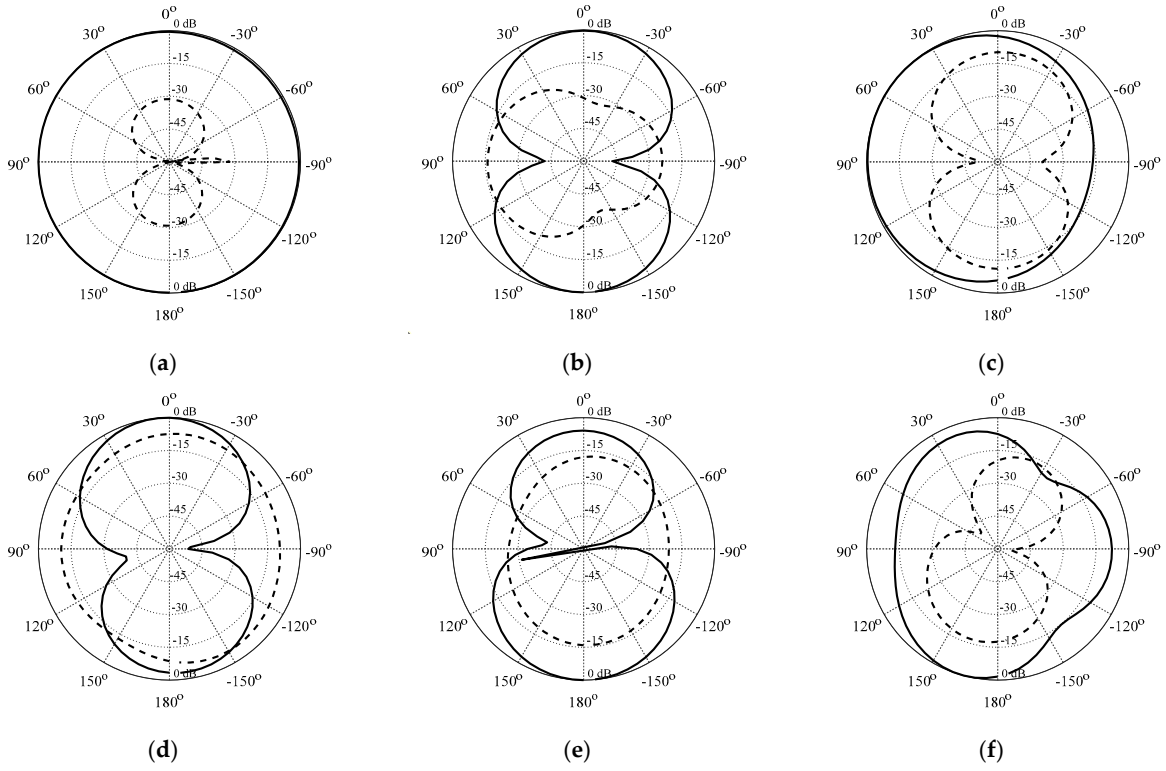

Figure 29. Radiation patterns (normalized directivity): (**a**) 4.0 GHz, *yz*-plane, (**b**) 4.0 GHz, *xz*-plane, (**c**) 6.0 GHz, *yz*-plane, (**d**) 6.0 GHz, *xz*-plane, (**e**) 8.0 GHz, *yz*-plane, and (**f**) 8.0 GHz, *xz*-plane. Co-pol and cross-pol patterns shown using the solid and dashed lines, respectively.

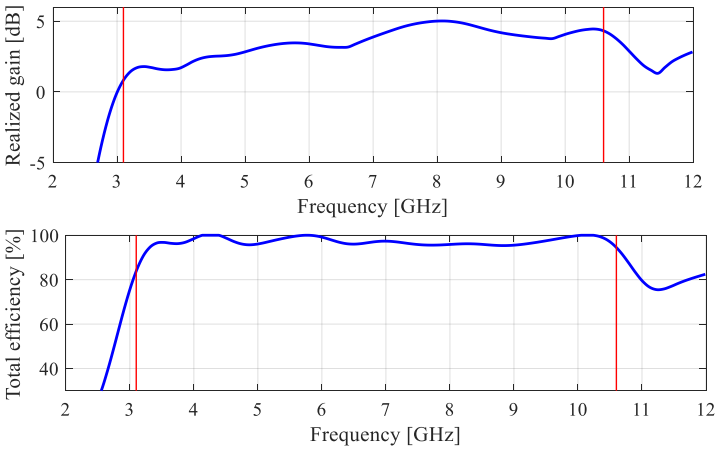

Figure 30. Realized gain and total efficiency of the antenna of Figure 28. Vertical lines mark the operating band.

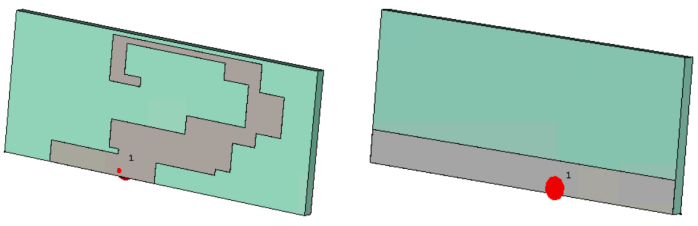

Figure 31. Illustration case V: 50 × 20 mm triple-band antenna with GSM band: (**a**) front view; (**b**) back view.

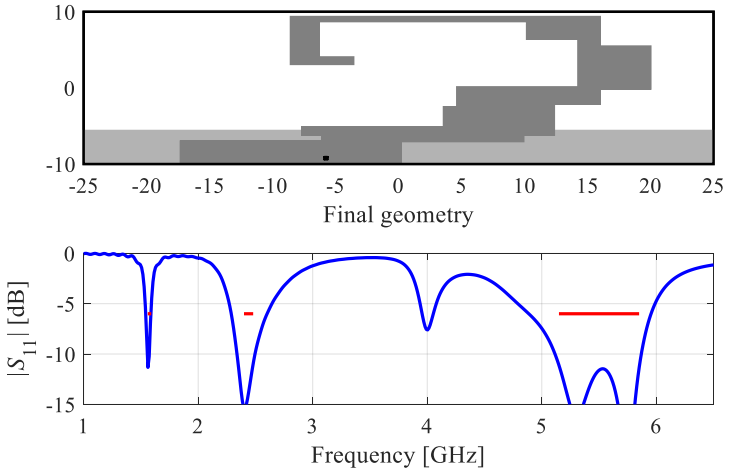

Figure 32. Case V: final antenna geometry (not in the right proportions) and the reflection response. Port location marked as the black circle. Light-gray shade marks the antenna ground. Horizontal lines mark target operating bands.

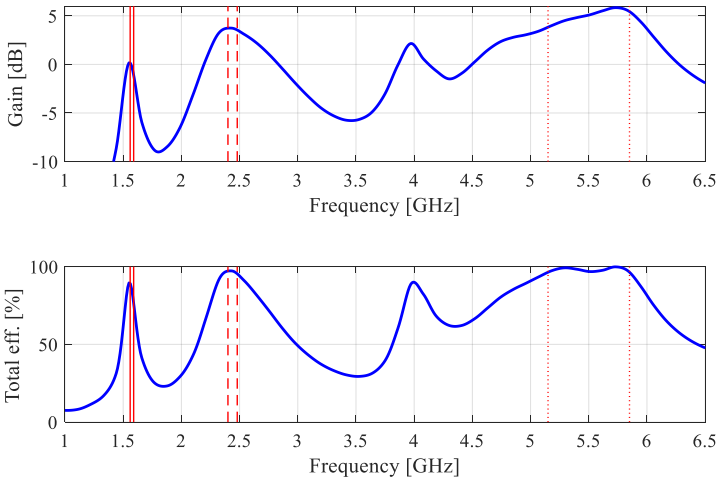

Figure 33. Realized gain and total efficiency of the antenna of Figure 32. Vertical lines mark the operating band.

3.6. Case VI

Our last example is a triple-band antenna implemented on 0.6 mm thick FR-4 substrate (ε_r = 4.4). The antenna size is only 36 × 5 mm, and it includes a metallic environment modeled as PEC. The total size of the structure is 80 × 10 mm, see Figure 35. The design specifications are $|S_{11}(\boldsymbol{x},f)| \leq -6$ dB for 2.40 $\leq f \leq$ 2.48 GHz, 5.15 $\leq f \leq$ 7.13 GHz, 7.75 $\leq f \leq$ 8.25 GHz. Note that this is an extremely tough case due to strict limits imposed on antenna footprint. The designed obtained using the framework of Section 2 has been shown in Figure 36. The realized gain and total efficiency are shown in Figure 37, whereas Figure 38 illustrates radiation patterns at 2.45 GHz, 6.15 GHz, and 8.0 GHz (centers of the respective operating bands). It can be noted that—in this case—the impedance matching specifications were not met for the middle band (the average $|S_{11}|$ is slightly above −6 dB therein), yet the antenna operates in all three bands. The average in-band efficiency is about 63% in the lower band, about 60% in the middle band, and 62% in the upper band, whereas the average in-band gain is around 0 dB in the lower band and around 0.5 dB in the remaining bands. Nevertheless, despite stringent requirements, our algorithm produced a design that is close to expectations, and probably as good as it can be under this challenging scenario.

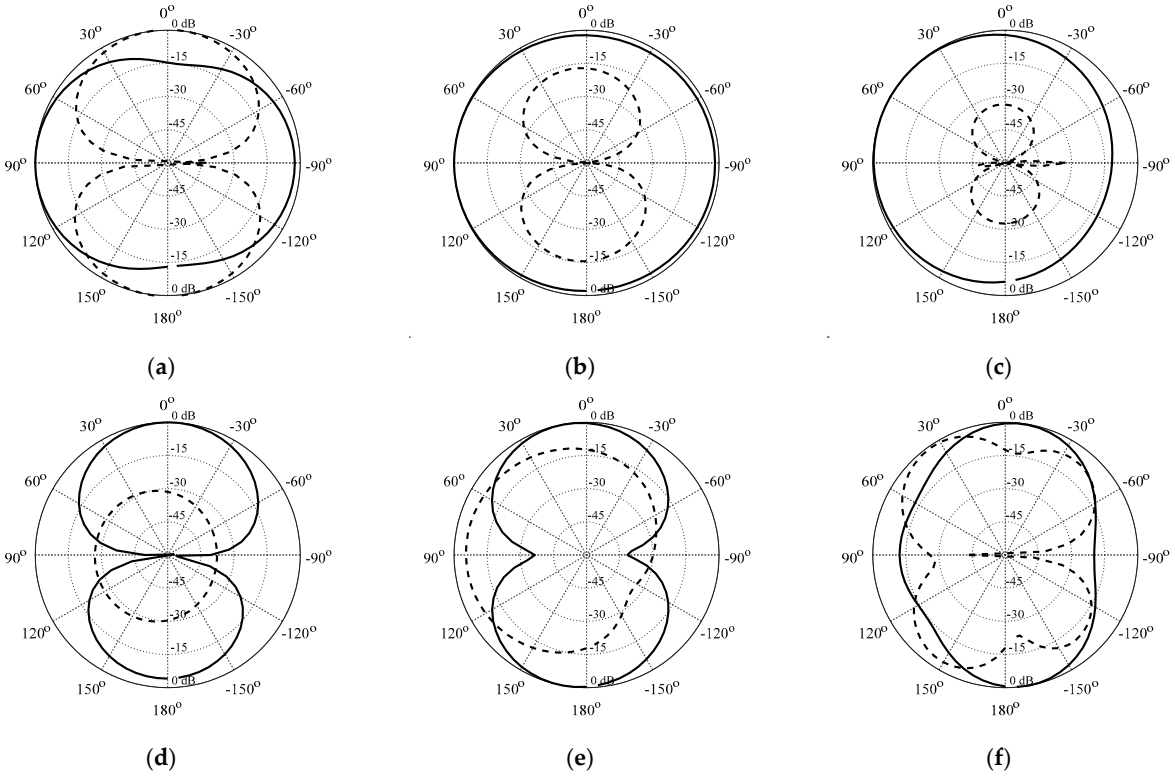

Figure 34. Radiation patterns (normalized directivity): (**a**) 1.575 GHz, *yz*-plane, (**b**) 1.575 GHz, *xz*-plane, (**c**) 2.45 GHz, *yz*-plane, (**d**) 2.45 GHz, *xz*-plane, (**e**) 5.5 GHz, *yz*-plane, and (**f**) 5.5 GHz, *xz*-plane. Co-pol and cross-pol patterns shown using the solid and dashed lines, respectively.

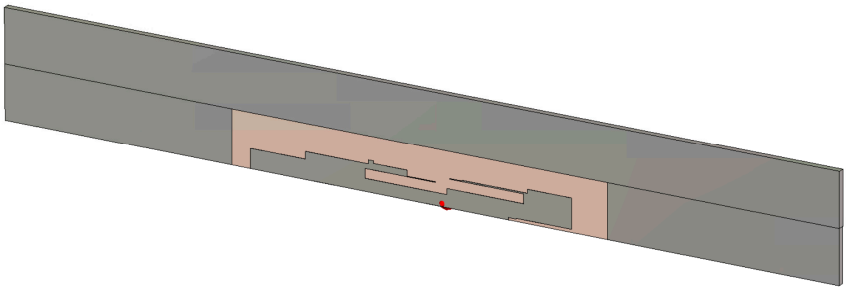

Figure 35. Illustration case VI: triple-band antenna with metallic environment.

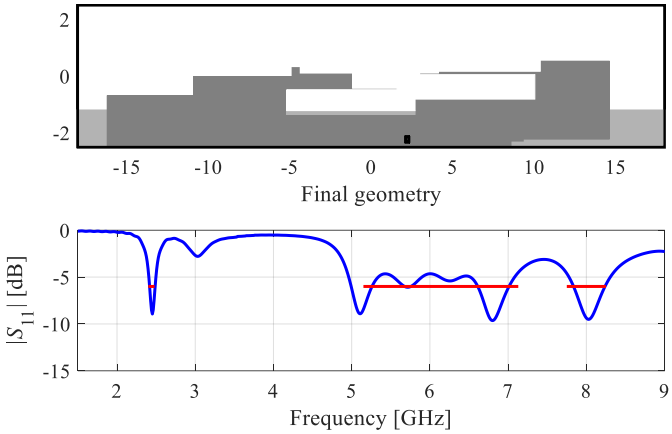

Figure 36. Case VI: final antenna geometry (not in the right proportions) and the reflection response. Port location marked as the black circle. Light-gray shade marks the antenna ground. Horizontal lines mark target operating bands.

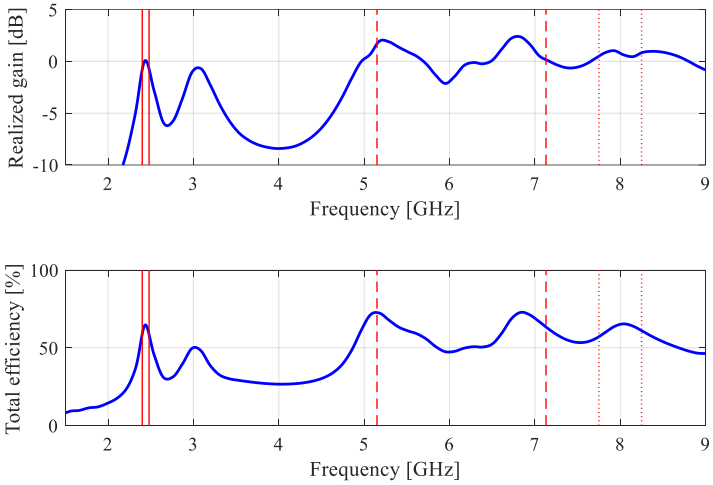

Figure 37. Realized gain and total efficiency of the antenna of Figure 36. Vertical lines mark the operating bands.

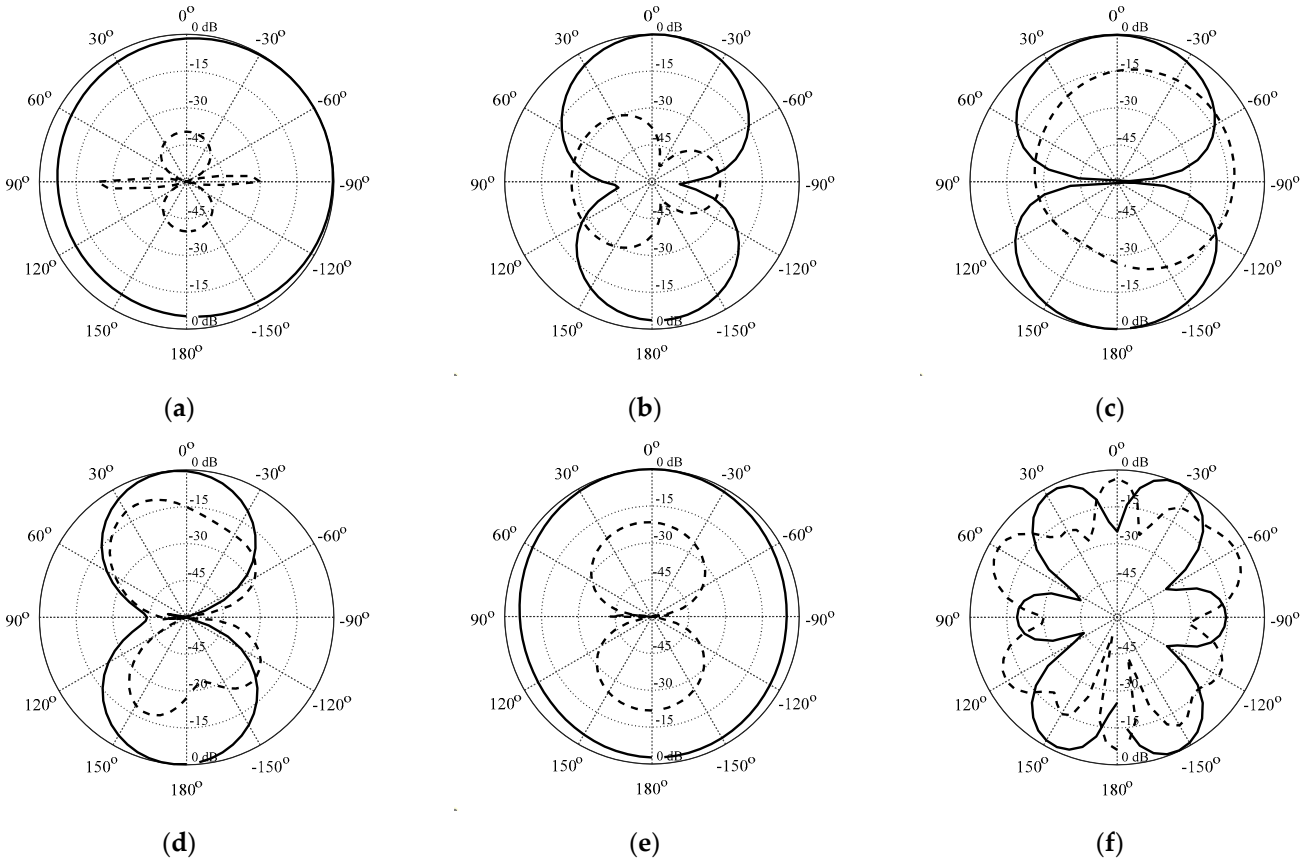

Figure 38. Radiation patterns (normalized directivity): (**a**) 2.45 GHz, *yz*-plane, (**b**) 2.45 GHz, *xz*-plane, (**c**) 6.15 GHz, *yz*-plane, (**d**) 6.15 GHz, *xz*-plane, (**e**) 8.0 GHz, *yz*-plane, (**f**) 8.0 GHz, *xz*-plane. Co-pol and cross-pol patterns shown using the solid and dashed lines, respectively.

For the sake of comparison, this case was re-performed with relaxed demands concerning miniaturization. The antenna size was enlarged to 45 × 6 mm while keeping the same metallic environment as before (thus, the total size of the structure is now 95 × 11 mm). The proposed framework generated the design that fulfils the prescribed specifications with a very slight violation of the matching requirements around 6.2 GHz, as shown in Figure 39.

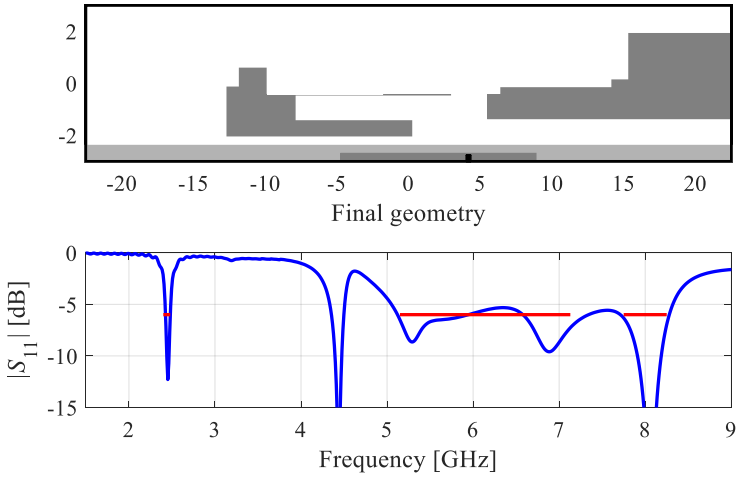

Figure 39. Case VI (relaxed size constraints, size of 45 × 6 mm): final antenna geometry (not in the right proportions) and the reflection response. Port location marked as the black circle. Light-gray shade marks the antenna ground. Horizontal lines mark target operating bands.

Figure 40 illustrates the realized gain and total efficiency responses. It can be observed that increasing antenna size leads to a dramatic improvement in the antenna performance. While the average total efficiency in the lower band is 65%, it is about 75% in the middle band and the upper band. At the same time, the realized gain increased to about 1 dB in the lower band, 2.5 dB in the middle band, and 3.5 dB in the upper band on the average. It should also be noticed that—as expected—the antenna geometry is entirely different to before.

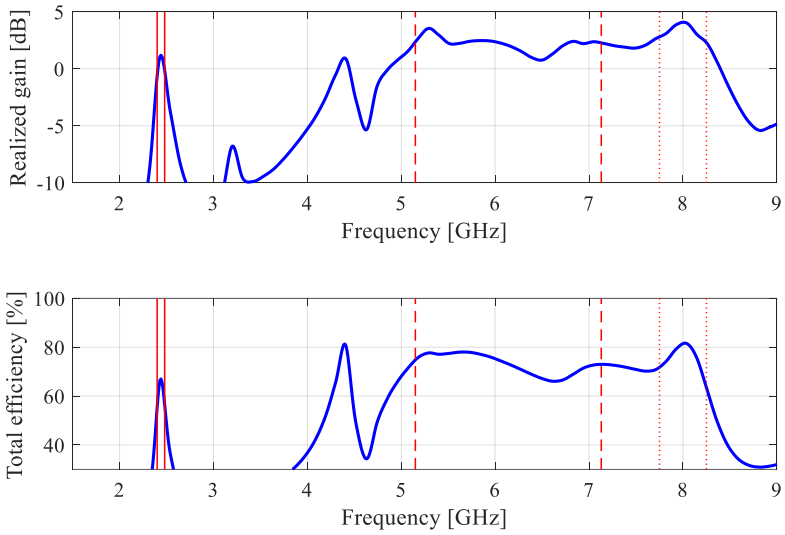

Figure 40. Realized gain and total efficiency of the antenna of Figure 39. Vertical lines mark the operating bands.

Further relaxing of size constraints, this time to 55 × 6 mm (the total structure size of 105 × 11 mm) leads to further improvement of antenna properties. Now, a structure has been generated that completely fulfils the specifications, as shown in Figure 41. Also, the average efficiency increases to 82% in the lower band, and almost 80% in the middle and upper band, whereas the average gain reaches 3.0 dB, 3.8 dB, and 3.5 dB in the lower, middle, and upper band, respectively (cf. Figure 42).

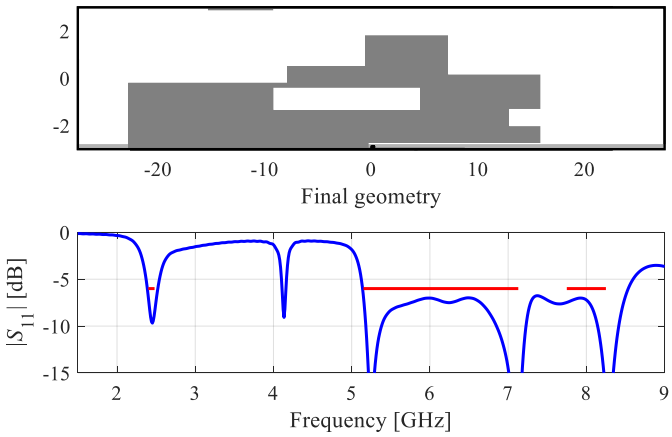

Figure 41. Case VI (relaxed size constraints, size of 55 × 6 mm): final antenna geometry (not in the right proportions) and the reflection response. Port location marked as the black circle. Light-gray shade marks the antenna ground. Horizontal lines mark target operating bands.

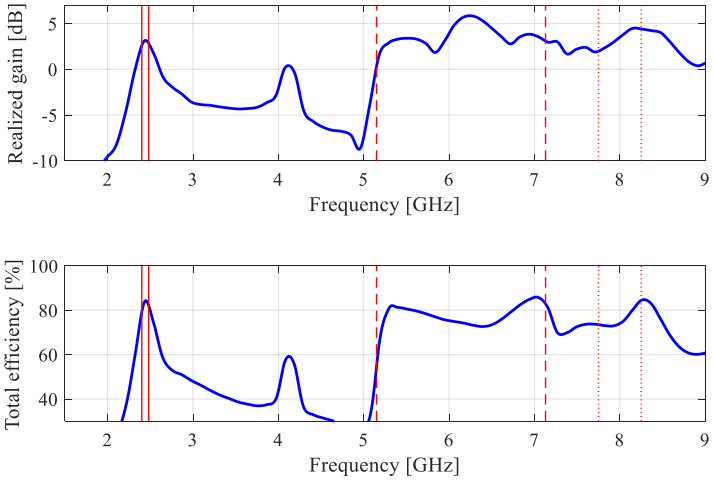

Figure 42. Realized gain and total efficiency of the antenna of Figure 41. Vertical lines mark the operating bands.

3.7. Experimental Validation

For the purpose of supplementary validation, selected antenna designs have been prototyped and measured in the anechoic chamber of Reykjavik University, Iceland. These include the triple-band antenna of Figure 23 (cf. Section 3.3), the ultra-wideband antenna of Figure 27 (cf. Section 3.4), and a triple-band antenna of Figure 31 (cf. Section 3.5). Figure 43 shows the photograph of the prototype of antenna of Figure 23, along with the EM-simulated and measured reflection and realized gain responses.

Figure 44 shows the H- and E-plane radiation patterns at 2.45 GHz, 6.15 GHz, and 8.0 GHz. Figure 45 shows the photograph of the prototype of antenna of Figure 27 and its EM-simulated and measured reflection and realized gain characteristics. Figure 46 provides the H- and E-plane radiation patterns at 4.0 GHz, 6.0 GHz, and 8.0 GHz. Finally, Figures 47 and 48 show the data (prototype photograph, reflection, gain, and radiation patterns at 1.575 GHz, 2.45 GHz, and 5.5 GHz) for the antenna of Figure 31. It can be observed that the agreement between the simulated and measured data is satisfactory in all cases. Minor discrepancies are mainly caused by fabrication and assembly inaccuracies. It should also be mentioned that the SMA connectors were not included in the computational models of the considered antenna structures. As these are compact devices, the presence of the connectors affects the electrical length of the ground planes, which may actually improve the antenna operation, especially in terms of impedance matching.

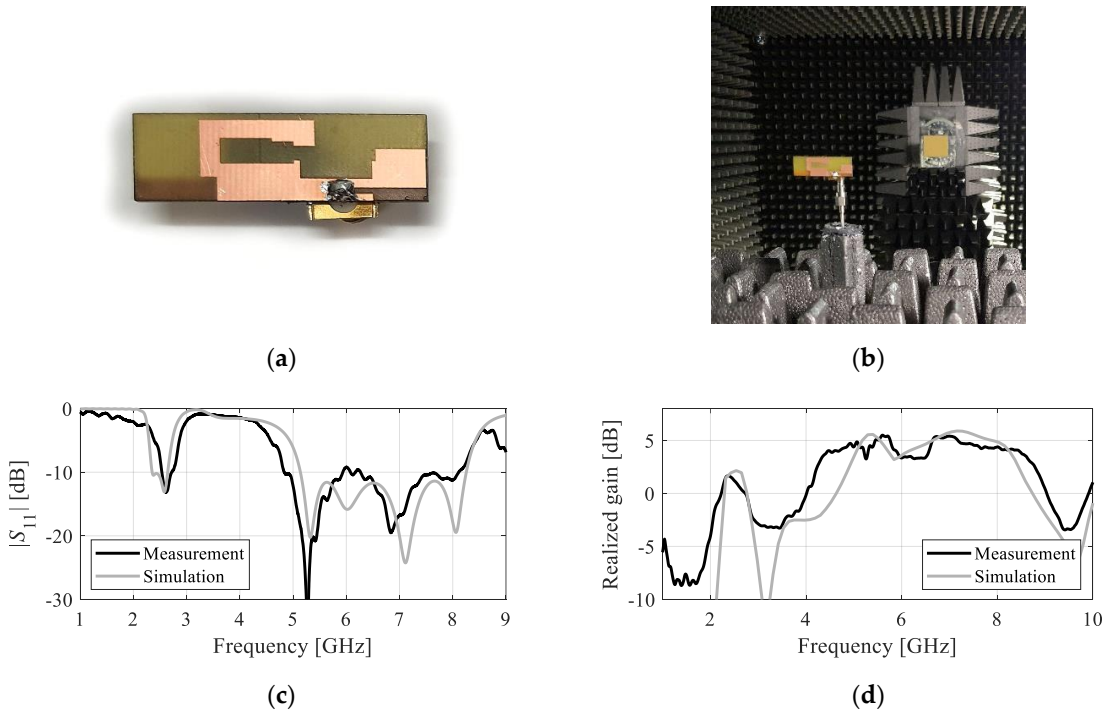

Figure 43. Experimental validation of the triple-band antenna of Figure 23: (**a**) prototype, (**b**) measurement setup, (**c**) simulated and measured reflection response, and (**d**) simulated and measured realized gain.

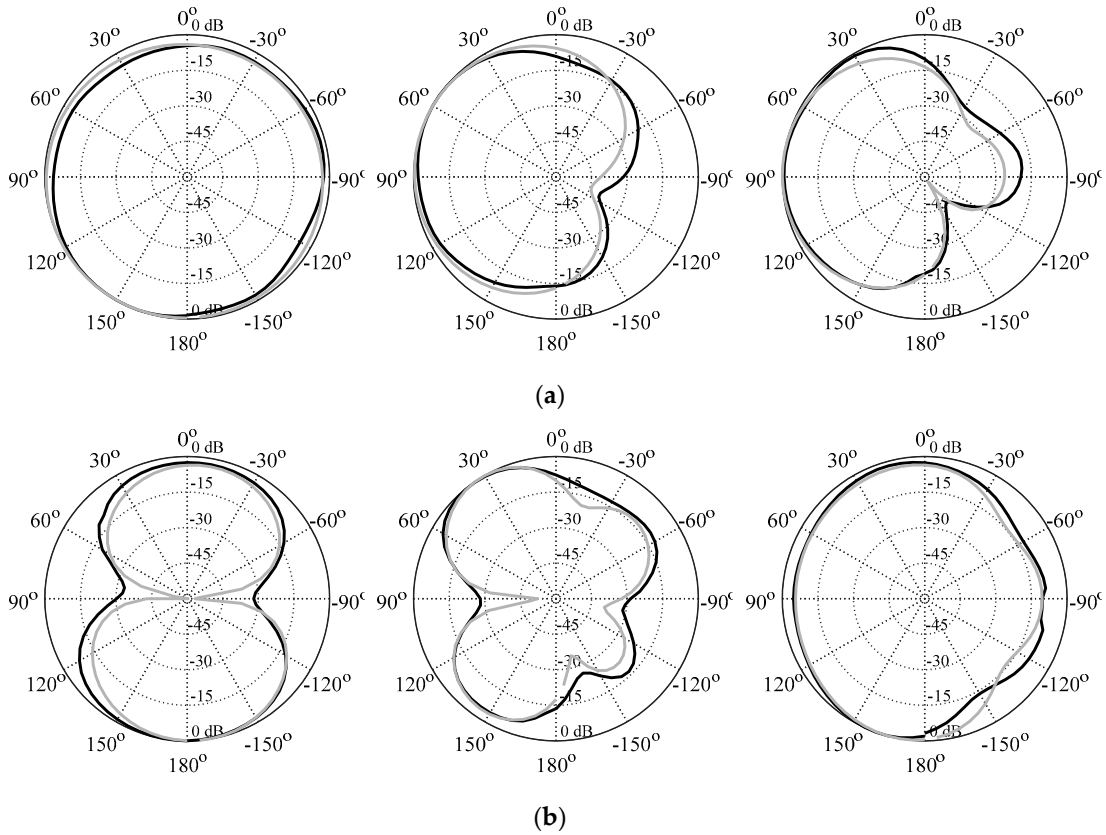

Figure 44. Experimental validation of the triple-band antenna of Figure 23: (**a**) simulated (gray) and measured (black) *yz*-plane patterns; (**b**) simulated (gray) and measured (black) *yz*-plane patterns. Patterns shown correspond to 2.45 GHz (**left**), 6.15 GHz (**middle**), and 8.0 GHz (**right**).

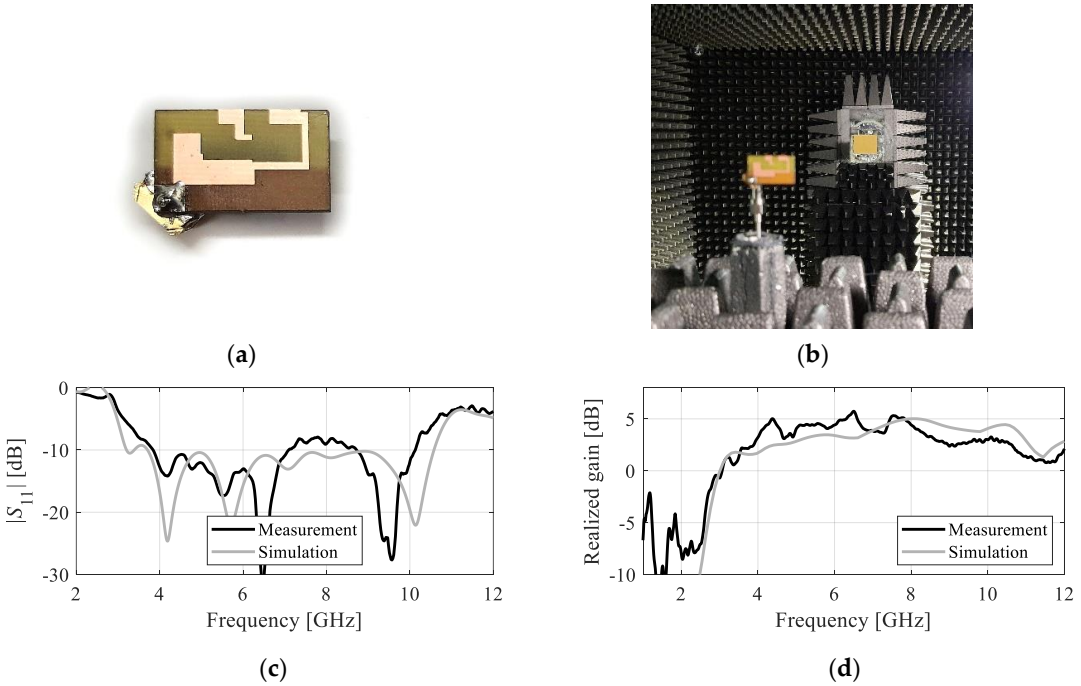

Figure 45. Experimental validation of the triple-band antenna of Figure 27: (**a**) prototype, (**b**) measurement setup, (**c**) simulated and measured reflection response, and (**d**) simulated and measured realized gain.

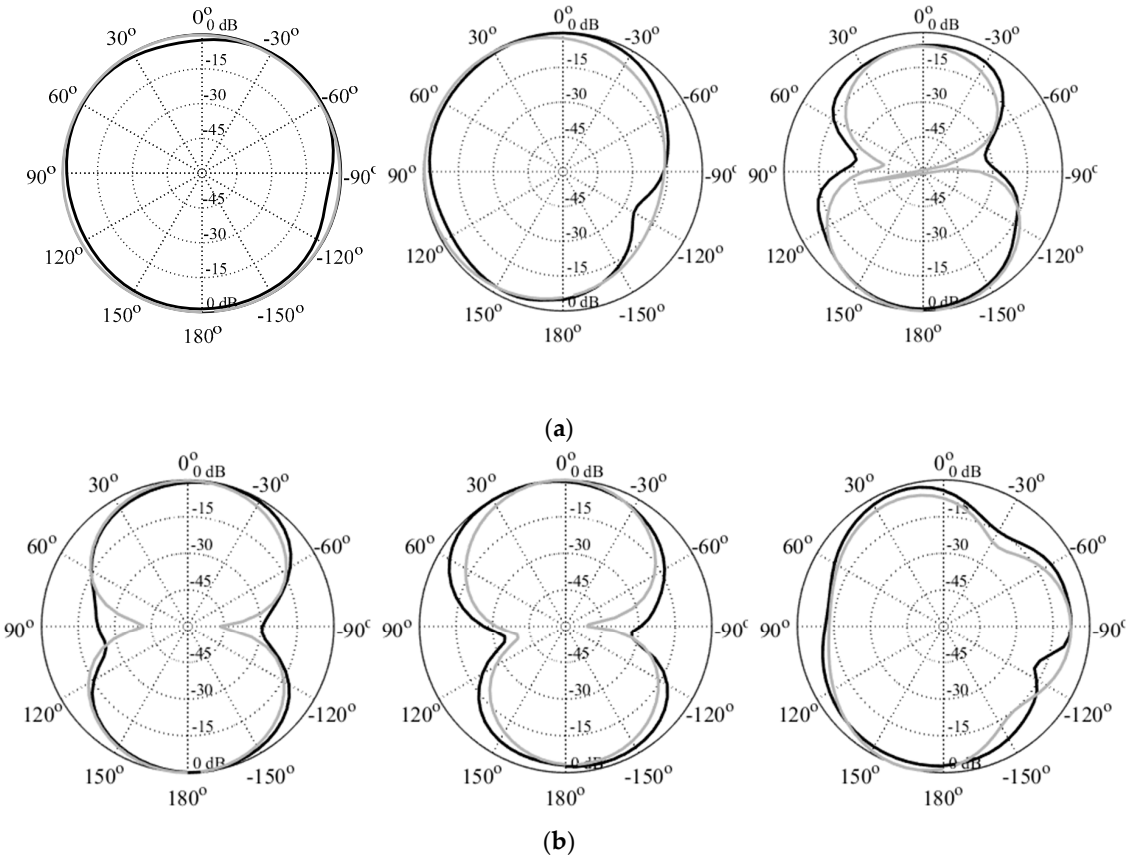

Figure 46. Experimental validation of the triple-band antenna of Figure 27: (**a**) simulated (gray) and measured (black) *yz*-plane patterns; (**b**) simulated (gray) and measured (black) *yz*-plane patterns. Patterns shown correspond to 4.0 GHz (**left**), 6.0 GHz (**middle**), and 8.0 GHz (**right**).

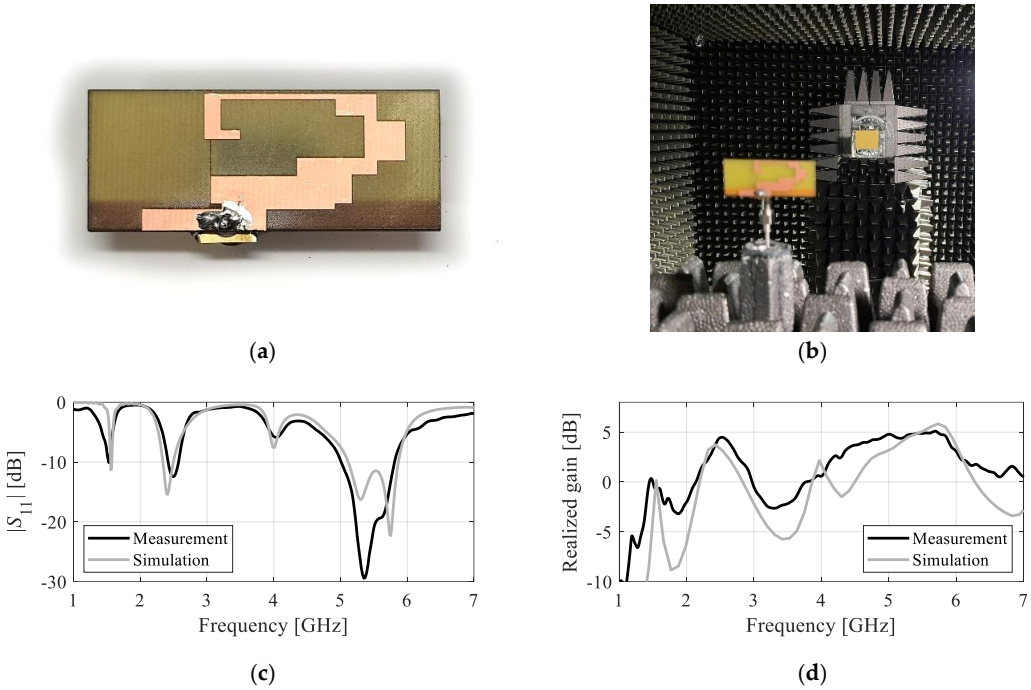

Figure 47. Experimental validation of the triple-band antenna of Figure 31: (**a**) prototype, (**b**) measurement setup, (**c**) simulated and measured reflection response, and (**d**) simulated and measured realized gain.

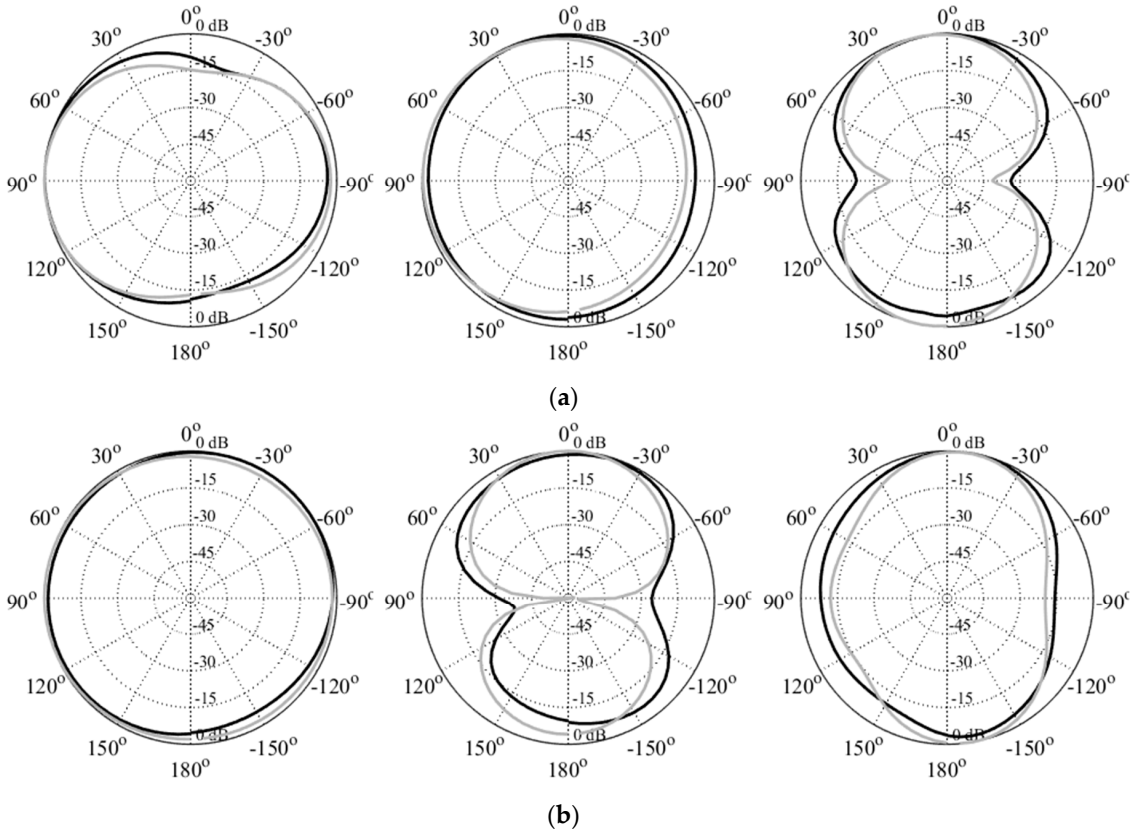

Figure 48. Experimental validation of the triple-band antenna of Figure 31: (**a**) simulated (gray) and measured (black) *yz*-plane patterns; (**b**) simulated (gray) and measured (black) *yz*-plane patterns. Patterns shown correspond to 1.575 GHz (**left**), 2.45 GHz (**middle**), and 5.5 GHz (**right**).

3.8. Discussion

The design scenarios discussed in this section demonstrate the versatility of the presented framework as well as its capability to generate antenna topologies for different design specifications (multi-band, broadband), and under challenging circumstances that include the presence of environmental components, and strict physical size constraints.

The design process is unsupervised and purely specification driven. Furthermore, the algorithmic tools are not tuned in any way for a particular problem at hand. On the contrary, the same setup has been utilized for all presented case studies. Our framework has been shown to be capable of yielding unconventional topologies, with specific geometrical components evolving to produce resonances at the target frequencies. The antennas are arranged to enable re-using their structural details at different frequency bands, thereby facilitating the fulfillment of the size constraints.

4. Conclusions

This paper proposed a novel algorithmic framework for automated and unsupervised development of planar antennas. Our methodology involves a generic and scalable parameterization that facilitates accommodating a large variety of possible antenna topologies while maintaining reasonably low dimensionality of the parameter space. Furthermore, the assumed parameterization can be used for combinatorial-optimization-based topology evolution (here, realized using nature-inspired procedures), and continuous-optimization-based fine-tuning of geometry parameters (here, carried out with an accelerated trust-region algorithm). Due to using simple building blocks (movable rectangular patches and holes), the resulting antenna structures are straightforward to fabricate.

The introduced framework has been validated through the design of several antenna structures under challenging scenarios, including multi-band operation with strict constraints imposed on the physical size of the radiator. In all cases, the same algorithmic setup has been used, meaning that the procedure has not been tuned to a particular problem at hand. At the same time, the computational cost of the design process is kept at levels which are acceptable in practice. The future work will focus on generalizing the framework (e.g., to permit design of 2.5D and 3D structures), as well as expediting the design process by incorporating surrogate modelling and machine learning tools.

The fundamental advantage of the proposed methodology is that it is unsupervised and specification driven. This means that no expert knowledge nor human interaction is required to develop and optimize the antenna structures. The presented approach is completely different to conventional methods, which normally start from known antenna topologies (patches, monopoles, inverted-F antennas, etc.) with designers attempting to introduce modifications that would lead to obtaining specific functionalities (e.g., multi-band operation). With the method proposed in the paper, an antenna topology is created automatically, and its dimensions are concurrently adjusted in the course of fully automated optimization process. One of its important benefits is that the proposed approach facilitates the development of very unconventional antenna topologies, which are unlikely to be developed by a human expert. Also, it is possible (as demonstrated through numerous examples) to design structures which are confined to specific dimensions, while exhibiting required functionality (e.g., dual-, triple-band or broadband operation).

Author Contributions: Conceptualization: S.K., J.Z. and W.D.; Data curation: P.R.; Formal analysis: S.K. and Y.T.; Funding acquisition: S.K., A.P.-D. and J.Z.; Methodology: S.K., A.C. and Y.T.; Project administration: S.K., W.D. and J.Z.; Resources: S.K., W.D. and J.Z.; Software: S.K.; Supervision: S.K., W.D. and J.Z.; Validation: S.K., A.P.-D. and P.R.; Visualization: S.K. and A.C.; Writing—original draft: S.K.; Writing—review and editing: S.K., A.P.-D., W.D., P.R., A.C., Y.T. and J.Z. All authors have read and agreed to the published version of the manuscript.

Funding: This paper is a joint research between academia (Reykjavik University) and industry (Meta Reality Labs). S. Koziel's work was partially supported by the Icelandic Centre for Research (RANNIS) Grant 239858 and by the National Science Centre of Poland Grant 2022/47/B/ST7/00072 through Engineering Optimization and Modeling Center of Reykjavik University and Faculty of Electronics, Telecommunications, and Informatics at Gdansk University of Technology.

Data Availability Statement: Data sharing is not applicable.

Conflicts of Interest: The authors declare no conflict of interest. The funders had no role in the design of the study; in the collection, analyses, or interpretation of data; in the writing of the manuscript; or in the decision to publish the results.

References

1. Hu, Y.; Qiu, Z.; Yang, B.; Shi, S.; Yang, J. Design of novel wideband circularly polarized antenna based on Vivaldi antenna structure. *IEEE Antennas Wirel. Prop. Lett.* **2015**, *14*, 1662–1665. [CrossRef]
2. Wen, D.; Hao, Y.; Munoz, M.O.; Wang, H.; Zhou, H. A compact and low-profile MIMO antenna using a miniature circular high-impedance surface for wearable applications. *IEEE Trans. Antennas Propag.* **2018**, *66*, 96–104. [CrossRef]
3. Lei, S.; Yang, Y.; Hu, H.; Zhao, Z.; Chen, B.; Qiu, X. Power gain optimization method for wide-beam array antenna via convex optimization. *IEEE Trans. Antennas Propag.* **2019**, *67*, 1620–1629. [CrossRef]
4. Wang, J.; Yang, X.S.; Wang, B.Z. Efficient gradient-based optimisation of pixel antenna with large-scale connections. *IET Microw. Antennas Prop.* **2018**, *12*, 385–389. [CrossRef]
5. Nagar, J.; Chaky, R.J.; Pantoja, M.F.; McKinley, A.F.; Werner, D.H. Optimization of far-field radiation from impedance-loaded nanoloops accelerated by an exact analytical formulation. *IEEE Trans. Antennas Prop.* **2019**, *67*, 1448–1458. [CrossRef]
6. Feng, F.; Zhang, J.; Zhang, W.; Zhao, Z.; Jin, J.; Zhang, Q.J. Coarse- and fine-mesh space mapping for EM optimization incorporating mesh deformation. *IEEE Microw. Wirel. Comp. Lett.* **2019**, *29*, 510–512. [CrossRef]
7. Pietrenko-Dabrowska, A.; Koziel, S. Computationally-efficient design optimization of antennas by accelerated gradient search with sensitivity and design change monitoring. *IET Microw. Antennas Prop.* **2020**, *14*, 165–170. [CrossRef]
8. Kolda, T.G.; Lewis, R.M.; Torczon, V. Optimization by direct search: New perspectives on some classical and modern methods. *SIAM Rev.* **2005**, *45*, 385–482. [CrossRef]
9. Li, X.; Luk, K.M. The grey wolf optimizer and its applications in electromagnetics. *IEEE Trans. Antennas Prop.* **2020**, *68*, 2186–2197. [CrossRef]
10. Luo, X.; Yang, B.; Qian, H.J. Adaptive synthesis for resonator-coupled filters based on particle swarm optimization. *IEEE Trans. Microw. Theory Tech.* **2015**, *67*, 712–725. [CrossRef]
11. Aldhafeeri, A.; Rahmat-Samii, Y. Brain storm optimization for electromagnetic applications: Continuous and discrete. *IEEE Trans. Antennas Prop.* **2019**, *67*, 2710–2722. [CrossRef]
12. Majumder, A.; Chatterjee, S.; Chatterjee, S.; Sinha Chaudhari, S.; Poddar, D.R. Optimization of small-signal model of GaN HEMT by using evolutionary algorithms. *IEEE Microw. Wirel. Comp. Lett.* **2017**, *27*, 362–364. [CrossRef]
13. Easum, J.A.; Nagar, J.; Werner, P.L.; Werner, D.H. Efficient multi-objective antenna optimization with tolerance analysis through the use of surrogate models. *IEEE Trans. Antennas Prop.* **2018**, *66*, 6706–6715. [CrossRef]
14. Wang, X.; Wang, G.; Wang, D.; Zhang, Q. Ensemble-learning-based multiobjective optimization for antenna design. *IEEE Trans. Antennas Propag.* **2023**, *71*, 1296–1303. [CrossRef]
15. Baumgartner, P.; Baurnfeind, T.; Biro, O.; Hackl, A.; Magele, C.; Renhart, W.; Torchio, R. Multi-objective optimization of Yagi-Uda antenna applying enhanced firefly algorithm with adaptive cost function. *IEEE Trans. Magn.* **2018**, *54*, 8000504. [CrossRef]
16. Du, J.; Roblin, C. Statistical modeling of disturbed antennas based on the polynomial chaos expansion. *IEEE Antennas Wirel. Prop. Lett.* **2017**, *16*, 1843–1847. [CrossRef]
17. Wu, Q.; Chen, W.; Yu, C.; Wang, H.; Hong, W. Multilayer machine learning-assisted optimization-based robust design and its application to antennas and array. *IEEE Trans. Antennas Propag.* **2021**, *69*, 6052–6057. [CrossRef]
18. Acikgoz, H.; Mittra, R. Stochastic polynomial chaos expansion analysis of a split-ring resonator at terahertz frequencies. *IEEE Trans. Antennas Propag.* **2018**, *66*, 2131–2134. [CrossRef]
19. Koziel, S.; Pietrenko-Dabrowska, A. Global EM-driven optimization of multi-band antennas using knowledge-based inverse response-feature surrogates. *Knowl. Based Syst.* **2021**, *227*, 107189. [CrossRef]
20. Hassan, A.K.S.O.; Etman, A.S.; Soliman, E.A. Optimization of a novel nano antenna with two radiation modes using kriging surrogate models. *IEEE Photon. J.* **2018**, *10*, 4800807. [CrossRef]
21. Feng, F.; Zhang, C.; Na, W.; Zhang, J.; Zhang, W.; Zhang, Q. Adaptive feature zero assisted surrogate–based EM optimization for microwave filter design. *IEEE Microw. Wirel. Comp. Lett.* **2019**, *29*, 2–4. [CrossRef]
22. Zhang, Z.; Chen, H.C.; Cheng, Q.S. Surrogate-assisted quasi-newton enhanced global optimization of antennas based on a heuristic hypersphere sampling. *IEEE Trans. Antennas Propag.* **2021**, *69*, 2993–2998. [CrossRef]
23. Dong, J.; Qin, W.; Wang, M. Fast multi-objective optimization of multi-parameter antenna structures based on improved BPNN surrogate model. *IEEE Access* **2019**, *7*, 77692–77701. [CrossRef]

24. Xiao, L.-Y.; Shao, W.; Iong Jin, F.; Wang, B.-Z. Multiparameter modeling with ANN for antenna design. *IEEE Trans. Antennas Propag.* **2018**, *66*, 3718–3723. [CrossRef]
25. Cui, L.; Zhang, Y.; Zhang, R.; Liu, Q.H. A modified efficient KNN method for antenna optimization and design. *IEEE Trans. Antennas Propag.* **2020**, *68*, 6858–6866. [CrossRef]
26. Bandler, J.W.; Cheng, Q.; Dakroury, S.A.; Mohamed, A.S.; Bakr, M.H.; Madsen, K.; Søndergaard, J. Space mapping: The state of the art. *IEEE Trans. Microw. Theory Tech.* **2004**, *52*, 337–361. [CrossRef]
27. Zhu, J.; Bandler, J.W.; Nikolova, N.K.; Koziel, S. Antenna optimization through space mapping. *IEEE Trans. Antennas Propag.* **2007**, *55*, 651–658. [CrossRef]
28. Cervantes-González, J.C.; Rayas-Sánchez, J.E.; López, C.A.; Camacho-Pérez, J.R.; Brito-Brito, Z.; Chávez-Hurtado, J.L. Space mapping optimization of handset antennas considering EM effects of mobile phone components and human body. *Int. J. RF Microw. CAE* **2016**, *26*, 121–128. [CrossRef]
29. Zhang, W.; Feng, F.; Liu, W.; Yan, S.; Zhang, J.; Jin, J.; Zhang, Q.J. Advanced parallel space-mapping-based multiphysics optimization for high-power microwave filters. *IEEE Trans. Microw. Theory Tech.* **2021**, *69*, 2470–2484. [CrossRef]
30. Wu, Q.; Wang, H.; Hong, W. Multistage collaborative machine learning and its application to antenna modeling and optimization. *IEEE Trans. Antennas Propag.* **2020**, *68*, 3397–3409. [CrossRef]
31. Alzahed, A.M.; Mikki, S.M.; Antar, Y.M.M. Nonlinear mutual coupling compensation operator design using a novel electromagnetic machine learning paradigm. *IEEE Antennas Wirel. Prop. Lett.* **2019**, *18*, 861–865. [CrossRef]
32. Torun, H.M.; Swaminathan, M. High-dimensional global optimization method for high-frequency electronic design. *IEEE Trans. Microw. Theory Techn.* **2019**, *67*, 2128–2142. [CrossRef]
33. Koziel, S.; Ogurtsov, S. Rapid design closure of linear microstrip antenna array apertures using response features. *IEEE Antennas Wirel. Prop. Lett.* **2018**, *17*, 645–648. [CrossRef]
34. Pietrenko-Dabrowska, A.; Koziel, S. Generalized formulation of response features for reliable optimization of antenna input characteristics. *IEEE Trans. Antennas Propag.* **2021**, *70*, 3733–3748. [CrossRef]
35. Zhang, C.; Feng, F.; Gongal-Reddy, V.; Zhang, Q.J.; Bandler, J.W. Cognition-driven formulation of space mapping for equal-ripple optimization of microwave filters. *IEEE Trans. Microw. Theory Techn.* **2015**, *63*, 2154–2165. [CrossRef]
36. Koziel, S.; Leifsson, L. *Simulation-Driven Design by Knowledge-Based Response Correction Techniques*; Springer: New York, NY, USA, 2016.
37. Koziel, S.; Unnsteinsson, S.D. Expedited design closure of antennas by means of trust-region-based adaptive response scaling. *IEEE Antennas Wirel. Propag. Lett.* **2018**, *17*, 1099–1103. [CrossRef]
38. Jacobs, J.P.; Koziel, S. Two-stage framework for efficient Gaussian process modeling of antenna input characteristics. *IEEE Trans. Antennas Prop.* **2014**, *62*, 706–713. [CrossRef]
39. Kennedy, M.C.; O'Hagan, A. Predicting the output from complex computer code when fast approximations are available. *Biometrika* **2000**, *87*, 1–13. [CrossRef]
40. Zhong, Y.; Renner, P.; Dou, W.; Ye, G.; Zhu, J.; Liu, Q.H. A machine learning generative method for automating antenna design and optimization. *IEEE J. Multiscale Multiphys. Comput. Tech.* **2022**, *7*, 285–295. [CrossRef]
41. Sharma, Y.; Zhang, H.H.; Xin, H. Machine learning techniques for optimizing design of double T-shaped monopole antenna. *IEEE Trans. Antennas Propag.* **2020**, *68*, 5658–5663. [CrossRef]
42. Chen, Y.-S.; Chiu, Y.-H. Application of multiobjective topology optimization to miniature ultrawideband antennas with enhanced pulse preservation. *IEEE Antennas Wirel. Propag. Lett.* **2016**, *15*, 842–845. [CrossRef]
43. Liu, P.; Chen, L.; Chen, Z.N. Prior-knowledge-guided deep-learning-enabled synthesis for broadband and large phase shift range metacells in metalens antenna. *IEEE Trans. Antennas Propag.* **2022**, *70*, 5024–5034. [CrossRef]
44. Ohira, M.; Ban, H.; Ueba, M. Evolutionary generation of subwavelength planar element loaded monopole antenna. *IEEE Antennas Wireless Propag. Lett.* **2011**, *10*, 1559–1562. [CrossRef]
45. Arianos, S.; Quijano, J.L.A.; Vipiana, F.; Dassano, G.; Vecchi, G.; Orefice, M. Application of evolutionary algorithms in the design of compact multi-band antennas. In Proceedings of the 2012 IEEE International Symposium on Antennas and Propagation, Chicago, IL, USA, 8–14 July 2012; pp. 1–2.
46. Bird, T.S. Design of antennas through optimization of geometry. In Proceedings of the 2013 5th IEEE International Symposium on Microwave, Antenna, Propagation and EMC Technologies for Wireless Communications, Chengdu, China, 29–31 October 2013; p. 1.
47. Jiang, F.; Chiu, C.-Y.; Shen, S.; Cheng, Q.S.; Murch, R. Pixel antenna optimization using N-port characteristic mode analysis. *IEEE Trans. Antennas Propag.* **2020**, *68*, 3336–3347. [CrossRef]
48. Soltani, S.; Lotfi, P.; Murch, R.D. Design and optimization of multiport pixel antennas. *IEEE Trans. Antennas Propag.* **2018**, *66*, 2049–2054. [CrossRef]
49. Lotfi, P.; Soltani, S.; Murch, R.D. Printed endfire beam-steerable pixel antenna. *IEEE Trans. Antennas Propag.* **2017**, *65*, 3913–3923. [CrossRef]
50. Song, S.; Murch, R.D. An efficient approach for optimizing frequency reconfigurable pixel antennas using genetic algorithms. *IEEE Trans. Antennas Propag.* **2014**, *62*, 609–620. [CrossRef]
51. Jiang, F.; Shen, S.; Chiu, C.Y.; Zhang, Z.; Zhang, Y.; Cheng, Q.S.; Murch, R. Pixel antenna optimization based on perturbation sensitivity analysis. *IEEE Trans. Antennas Propag.* **2022**, *70*, 472–486. [CrossRef]

52. Zhu, S.-H.; Yang, X.-S.; Wang, J.; Wang, B.-Z. Design of MIMO antenna isolation structure based on a hybrid topology optimization method. *IEEE Trans. Antennas Propag.* **2018**, *67*, 6298–6307. [CrossRef]
53. Hassan, E.; Noreland, D.; Augustine, R.; Wadbro, E.; Berggren, M. Topology optimization of planar antennas for wideband near-field coupling. *IEEE Trans. Antennas Propag.* **2015**, *63*, 4208–4213. [CrossRef]
54. Hassan, E.; Wadbro, E.; Berggren, M. Topology optimization of metallic antennas. *IEEE Trans. Antennas Propag.* **2014**, *62*, 2488–2500.
55. Wang, J.; Yang, X.-S.; Ding, X.; Wang, B.-Z. Topology optimization of conical-beam antennas exploiting rotational symmetry. *IEEE Trans. Antennas Propag.* **2018**, *66*, 2254–2261. [CrossRef]
56. Erentok, A.; Sigmund, O. Topology optimization of sub-wavelength antennas. *IEEE Trans. Antennas Propag.* **2011**, *59*, 58–69. [CrossRef]
57. Mori, T.; Murakami, R.; Sato, Y.; Campelo, F.; Igarashi, H. Shape optimization of wideband antennas for microwave energy harvesters using FDTD. *IEEE Trans. Antennas Propag.* **2015**, *51*, 8000804. [CrossRef]
58. Wang, J.; Yang, X.-S.; Ding, X.; Wang, B.-Z. Antenna radiation characteristics optimization by a hybrid topological method. *IEEE Trans. Antennas Propag.* **2017**, *65*, 2843–2854. [CrossRef]
59. Naseri, P.; Hum, S.V. A generative machine learning-based approach for inverse design of multilayer metasurfaces. *IEEE Trans. Antennas Propag.* **2021**, *69*, 5725–5739. [CrossRef]
60. *CST Microwave Studio*, version 2021; Dassault Systemes: Vélizy-Villacoublay, France, 2021.
61. Michalewicz, Z. *Genetic Algorithms + Data Structures = Evolution Programs*; Springer: New York, NY, USA, 1996.
62. Blickle, T.; Thiele, L. A comparison of selection schemes used in evolutionary algorithms. *Evol. Comp.* **1996**, *4*, 361–394. [CrossRef]
63. Conn, A.R.; Gould, N.I.M.; Toint, P.L. *Trust Region Methods*; MPS-SIAM Series on Optimization; Society for Industrial and Applied Mathematics: Philadelphia, PA, USA, 2000.
64. Levy, V.; Lessman, F. *Finite Difference Equations*; Dover Publications Inc.: New York, NY, USA, 1992.
65. Nocedal, J.; Wright, S.J. *Numerical Optimization*, 2nd ed.; Springer: New York, NY, USA, 2006.
66. *Matlab*, version 2021a; MathWorks Inc.: Natick, MA, USA, 2021.
67. Pietrenko-Dabrowska, A.; Koziel, S. Numerically efficient algorithm for compact microwave device optimization with flexible sensitivity updating scheme. *Int. J. RF Microw. CAE* **2019**, *29*, e21714. [CrossRef]